JCB Journal of Cell Biology

ARTICLE

Synaptic neurexin-1 assembles into dynamically regulated active zone nanoclusters

Justin H. Trotter[1,2]*, Junjie Hao[3,4,5]*, Stephan Maxeiner[1,2], Theodoros Tsetsenis[1,2], Zhihui Liu[1,2], Xiaowei Zhuang[3,4,5], and Thomas C. Südhof[1,2]

Neurexins are well-characterized presynaptic cell adhesion molecules that engage multifarious postsynaptic ligands and organize diverse synapse properties. However, the precise synaptic localization of neurexins remains enigmatic. Using super-resolution microscopy, we demonstrate that neurexin-1 forms discrete nanoclusters at excitatory synapses, revealing a novel organizational feature of synaptic architecture. Synapses generally contain a single nanocluster that comprises more than four neurexin-1 molecules and that also includes neurexin-2 and/or neurexin-3 isoforms. Moreover, we find that neurexin-1 is physiologically cleaved by ADAM10 similar to its ligand neuroligin-1, with ∼4–6% of neurexin-1 and ∼2–3% of neuroligin-1 present in the adult brain as soluble ectodomain proteins. Blocking ADAM10-mediated neurexin-1 cleavage dramatically increased the synaptic neurexin-1 content, thereby elevating the percentage of Homer1(+) excitatory synapses containing neurexin-1 nanoclusters from 40–50% to ∼80%, and doubling the number of neurexin-1 molecules per nanocluster. Taken together, our results reveal an unexpected nanodomain organization of synapses in which neurexin-1 is assembled into discrete presynaptic nanoclusters that are dynamically regulated via ectodomain cleavage.

Introduction

Synapses are specialized intercellular junctions that are dedicated to the transfer of information between neurons. Synaptic properties, such as release probability, postsynaptic receptor composition, and short-term synaptic plasticity, vary widely and are subject to activity-dependent short- and long-term changes (Abbott and Regehr, 2004; Bromer et al., 2018). These properties are determined by interactions between pre- and postsynaptic neurons that may be largely shaped by trans-synaptic cell adhesion molecules (Reyes et al., 1998; Somogyi et al., 1998; Koester and Johnston, 2005; Sheng and Kim, 2011; Siddiqui and Craig, 2011), including neurexins, which are arguably the best characterized (Südhof, 2017).

Neurexins are encoded by three genes, each of which contains independent promoters that drive transcription of longer α-neurexin and shorter β-neurexin proteins (Ushkaryov et al., 1992, 1994; Ushkaryov and Südhof, 1993; Fig. 1 A). The large extracellular sequence of α-neurexins includes six laminin/neurexin/sex hormone–binding globulin (LNS) domains with interspersed EGF-like repeats, while the extracellular sequence of β-neurexins contains only a short β-specific N-terminal sequence that splices into the α-neurexin sequence N-terminal to their sixth LNS domain (Fig. 1 A). Following the sixth LNS domain, α- and β-neurexins include a heavily glycosylated "stalk" region that is interrupted by a cysteine-loop domain, a transmembrane region, and a cytoplasmic tail. The neurexin-1 gene (*Nrxn1*) also encodes a third, shorter isoform called neurexin-1γ (Nrxn1γ) that is absent from the neurexin-2 (*Nrxn2*) and neurexin-3 (*Nrxn3*) genes and lacks LNS domains (Yan et al., 2015; Sterky et al., 2017; Fig. 1 A).

Due to alternative splicing, neurexins are differentially expressed as thousands of isoforms throughout the brain (Ullrich et al., 1995; Schreiner et al., 2014; Treutlein et al., 2014). Neurexins are presynaptic proteins that interact with a myriad of postsynaptic ligands, often in a manner regulated by alternative splicing, to perform multiple functions at synapses (Südhof, 2017). These functions likely depend on the specific isoforms expressed and on the ligands available, and include regulation of presynaptic Ca^{2+} channels (Missler et al., 2003; Chen et al., 2017), trans-synaptic recruitment of postsynaptic α-amino-3-hydroxy-5-methyl-4-isoxazolepropionic acid receptors (AMPARs)

[1]Department of Molecular and Cellular Physiology, Stanford University, Stanford, CA; [2]Howard Hughes Medical Institute, Stanford University, Stanford, CA; [3]Department of Chemistry and Chemical Biology, Harvard University, Cambridge, MA; [4]Department of Physics, Harvard University, Cambridge, MA; [5]Howard Hughes Medical Institute, Harvard University, Cambridge, MA.

*J.H. Trotter and J. Hao contributed equally to this paper; Correspondence to Thomas C. Südhof: tcs1@stanford.edu; Xiaowei Zhuang: zhuang@chemistry.harvard.edu; S. Maxeiner's present address is Fachbereich Anatomie und Zellbiologie, Universität des Saarlandes, Saarland, Germany; T. Tsetsenis's present address is Department of Neuroscience, University of Pennsylvania, Philadelphia, PA.

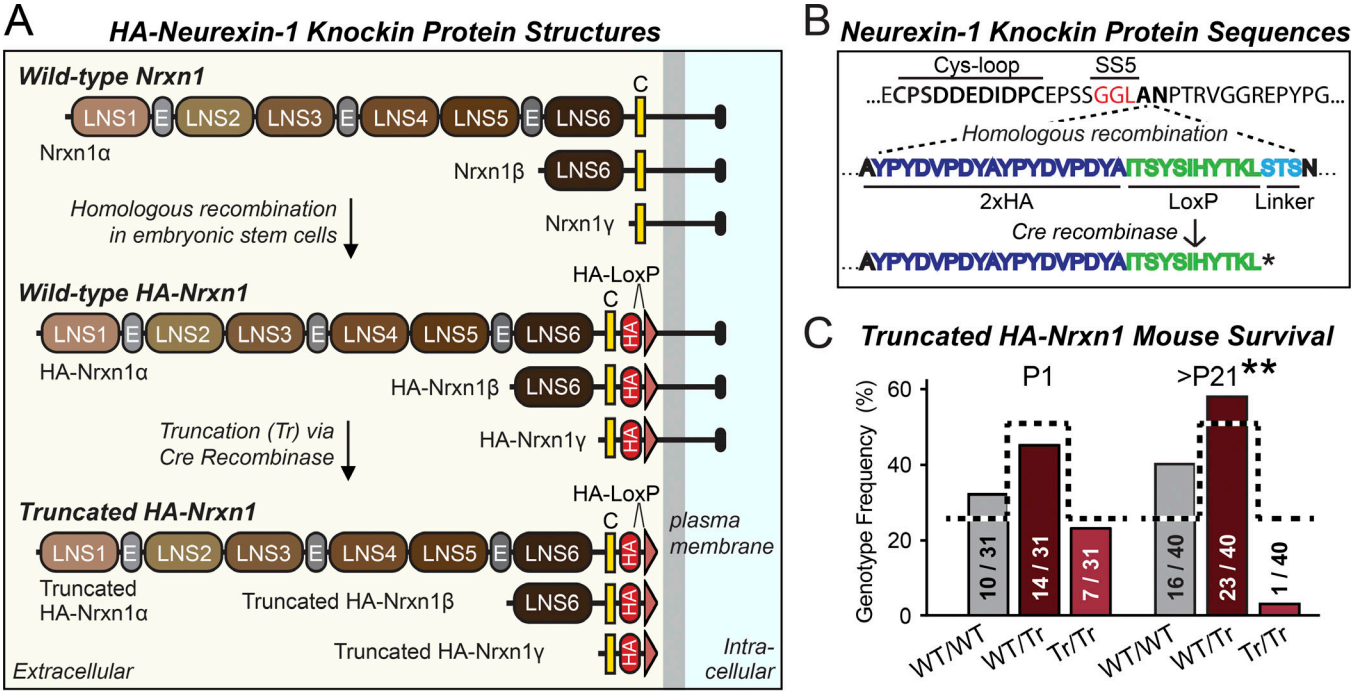

Figure 1. **Schematic of the *Nrxn1* cKI mice and impaired survival following constitutive truncation of *Nrxn1*. (A)** Diagram of WT, HA-tagged full-length, and HA-tagged truncated Nrxn1α, Nrxn1β, and Nrxn1γ. Top: WT Nrxn1 proteins. Middle: Nrxn1 proteins containing inserted tandem HA-epitopes and loxP sequences in cKI mice. Bottom: Truncated HA-tagged Nrxn1 proteins after Cre recombination (LNS1–6, LNS1-6 domains; E, EGF-like domain; C, cysteine-loop domain). **(B)** Amino acid sequences of the juxtamembranous region of WT Nrxn1 (top), Nrxn1 with the HA-epitope/loxP site knockin (middle), and Cre recombined truncated Nrxn1 (bottom; SS5 = alternative SS5). **(C)** Constitutive *Nrxn1* truncation impairs postnatal survival as analyzed in newborn (P1) and 21-d old mouse (P21) offspring from heterozygous matings. Statistical significance was assessed by the chi-square test (**, $P < 0.01$). For further details, see Fig. S1.

(Aoto et al., 2013) or N-methyl-D-arginine–type glutamate receptors (Dai et al., 2019), and control of tonic postsynaptic endocannabinoid synthesis (Anderson et al., 2015).

Recent studies have uncovered that synapses contain nanocolumns (Choquet and Triller, 2013; Maglione and Sigrist, 2013; Biederer et al., 2017; Chen et al., 2018; Hruska et al., 2018). Specifically, presynaptic release sites and postsynaptic receptors were shown to cluster into nanocolumns that are aligned across the synaptic cleft (Park et al., 2012; MacGillavry et al., 2013; Nair et al., 2013; Tang et al., 2016; Maschi and Klyachko, 2017). A different organization was observed for SynCams and N-cadherin, which are trans-synaptic cell adhesion molecules that were localized to a ring surrounding the active zone (Uchida et al., 1996; Perez de Arce et al., 2015). How other synaptic cell adhesion molecules, such as neurexins, are organized, however, remains unknown. Trans-synaptic signaling by synaptic cell adhesion molecules is likely dynamic, as suggested by the observation that these molecules are often substrates of ectodomain proteases such as ADAM10 and BACE1 (Kuhn et al., 2012, 2016; Prox et al., 2013). Cleavage by ectodomain proteases could provide a mechanism for the rapid and regulated disassembly of trans-synaptic protein complexes and for fine-tuning of synaptic properties. Indeed, this mechanism has been suggested for the neurexin ligand neuroligin-1, which is proteolytically processed by ADAM10 (Suzuki et al., 2012) and/or MMP9 (Peixoto et al., 2012).

In the present study, we analyzed Nrxn1 localization by 3D stochastic optical reconstruction microscopy (STORM; Rust et al., 2006; Huang et al., 2008). We found that at Homer1(+) excitatory synapses, Nrxn1 is localized to discrete nanoclusters that occupy a fraction of the synapse area and increase in neurexin content and physical size during synapse development. Moreover, we found that Nrxn1 is physiologically cleaved by ADAM10, thereby releasing a soluble fragment containing most of the extracellular sequences of Nrxn1. Inhibition of Nrxn1 cleavage by pharmacological blockage of ADAM10 dramatically enhances the Nrxn1 content of synaptic nanoclusters, and elevates the proportion of excitatory synapses containing Nrxn1 nanoclusters to nearly 100%. Taken together, our results reveal an unexpected nanoscale organization of synapses in which Nrxn1 is assembled into nanoclusters that are dynamically regulated by ADAM10 and may serve as a functional pivot for synapse specification.

Results

Generation of conditional knockin (cKI) mice expressing HA-tagged Nrxn1

To enable precise localization and monitoring of synaptic Nrxn1, we generated cKI mice that express HA-tagged Nrxn1 (Fig. 1, A and B; and Fig. S1 A). Specifically, we inserted a double HA-epitope tag and loxP sequence into the extracellular stalk region of Nrxn1 between the Cys-loop domain and the transmembrane

region (Fig. 1, A and B). In the *Nrxn1* gene, this region is encoded by the last coding exon that is 3′ to alternatively spliced sequence #5 (SS5; Fig. 1, A and B; and Fig. S1 A). In addition, we introduced a second loxP sequence into the 3′ noncoding region of the targeted exon. With this design, the *Nrxn1* cKI gene encodes full-length, HA-tagged Nrxn1 proteins in the absence of Cre-recombinase. Following Cre recombination, however, the *Nrxn1* cKI gene synthesizes truncated Nrxn1 proteins that are still HA-epitope tagged but lack a transmembrane region (Fig. 1 A). We chose this cKI design for studying Nrxn1 because we could find no neurexin antibodies that are specific for a given neurexin isoform, target extracellular sequences of a neurexin, and recognize native neurexins in cells or tissue. Moreover, this design replicates a strategy we employed in human neurons to model a *NRXN1* mutation associated with schizophrenia (Gauthier et al., 2011; Pak et al., 2015).

We crossed the *Nrxn1* cKI mice with transgenic mice expressing Cre-recombinase in the germ line, and analyzed the survival of the resulting constitutive truncated Nrxn1 (Nrxn1-Tr) mice. Homozygous Nrxn1-Tr mice were viable at birth, but only 1 in 40 mice survived until weaning (Fig. 1 C). mRNA measurements in brains from littermate WT and heterozygous Nrxn1-Tr mice suggest that the truncation mutation does not cause nonsense-mediated decay of the *Nrxn1* mRNAs (Fig. S1, B and C). Thus, while truncation disables Nrxn1 functions that are essential for survival, the epitope-tag itself does not seem to have a deleterious effect.

Hippocampal neurons cultured from HA-Nrxn1 cKI mice were infected with lentiviruses expressing mutant inactive (ΔCre; control) or active Cre-recombinase (Cre). After Cre expression, >95% of the *Nrxn1* cKI gene was recombined (Fig. S1 D). Neurons were live surface labeled with an HA antibody (Field et al., 1988), fixed and permeabilized, followed by labeling with a different HA antibody to visualize intracellular Nrxn1 and with an antibody to MAP2 to visualize dendrites (Fig. 2 A). We detected a punctate surface-staining pattern of HA-Nrxn1 in ΔCre-expressing neurons juxtaposed to dendrites, but found no HA-Nrxn1 puncta in Cre-expressing neurons. Intracellular HA-Nrxn1, conversely, was concentrated in the perinuclear region of neuronal somas and to a lesser extent in proximal primary dendrites (Fig. 2 A). Co-labeling of surface HA-Nrxn1 with synaptic markers revealed that some, but not all, synapses were associated HA-Nrxn1 (Fig. 2 A and Fig. S1 E).

We next analyzed cellular and secreted proteins in hippocampal neurons following Cre recombination via quantitative immunoblotting (Fig. 2 B). Consistent with the alternative splicing of *Nrxn1* mRNAs and glycosylation of Nrxn1 protein (Ushkaryov et al., 1994; Ullrich et al., 1995; Zhang et al., 2018), we observed in ΔCre-expressing neurons multiple cellular HA-Nrxn1α species (Fig. 2 B). In contrast, we detected in Cre-recombinase–expressing neurons a smaller Nrxn1α protein that was less abundant. No other cellular protein analyzed was changed. When we examined secreted proteins, we detected HA-tagged Nrxn1α in the medium of ΔCre-expressing neurons that was smaller than full-length cellular Nrxn1α (Fig. 2 B). In Cre-expressing neurons, truncated HA-tagged Nrxn1α was slightly smaller than its WT counterpart in ΔCre-expressing neurons and was found at lower levels, suggesting that Nrxn1 may be cleaved at a significant rate to produce secreted extracellular fragments.

Overall, these findings demonstrate that HA-tagged Nrxn1 expressed in *Nrxn1* cKI mice is functional, transported to the surface, and concentrated in puncta that are at least partly synaptic, but is also partly converted into a secreted protein. Conditional truncation of Nrxn1, conversely, produces only a secreted protein that is not functional and is present at lower levels, possibly because it is unstable (Pak et al., 2015).

Nrxn1 localizes to unique nanoclusters at synaptic junctions

To examine where in a synapse Nrxn1 is localized, we co-labeled HA-Nrxn1 and Homer1, an excitatory postsynaptic scaffolding protein (Xiao et al., 1998), using direct and indirect immunofluorescence, respectively, on cultured hippocampal neurons and cryostat sections within the stratum radiatum of the hippocampal CA1 region. We then imaged synapses using 3D STORM, a super-resolution imaging method (Rust et al., 2006; Huang et al., 2008).

Instead of being evenly distributed across the synaptic junction, Nrxn1 was concentrated in the synaptic cleft in discrete nanoclusters (Fig. 3, A, B, G, and H; and Fig. S1, F and G). Only a subset of Homer1(+) synapses contained Nrxn1 nanoclusters, and those with Nrxn1 nanoclusters mostly featured a single nanocluster (Fig. 3, C and I). Nrxn1 nanoclusters were similarly observed when we double labeled synapses for Nrxn1 and the presynaptic markers Piccolo (Fig. S1 F) or Bassoon (Fig. S1 G). Supporting the specificity of the HA antibodies, we did not observe HA(+) signals in Nrxn1 cKI neurons expressing Cre (Fig. S1 H) or in neurons or brain sections from WT mice (Fig. S1, I and J).

Because the synaptic images were acquired in 3D, we could rotate them to facilitate spatial analyses (Fig. 3, B and H). Quantifications showed that the distance between the Nrxn1 nanocluster and Homer1 disc along the trans-synaptic axis was similar in cultured hippocampal neurons and hippocampal sections (Fig. 3, D and J). We repeated these measurements using multiple synaptic marker proteins, and determined the position of Nrxn1 clusters relative to the synaptic cleft along the trans-synaptic axis based on the previously reported localizations of the same synaptic marker proteins (Dani et al., 2010). Using this approach, we localized the Nrxn1 HA-epitope to the presynaptic border of the synaptic cleft (Fig. 3 L), consistent with the juxtamembranous placement of the HA-epitope (Fig. 1 A).

Further quantifications revealed that each Nrxn1 nanocluster occupied ∼15–20% of the area of the synaptic cleft (Fig. 3, E and K), with 8.6 ± 0.6 primary antibodies bound to each nanocluster in cultured hippocampal neurons (Fig. 3 F). Since maximally two antibodies can bind to a HA-tagged Nrxn1 molecule, each nanocluster contains at least ∼4.3 Nrxn1 molecules, although the actual number is likely higher because not all epitopes will be saturated with antibodies.

Development of synaptic Nrxn1 nanoclusters

To study the development of Nrxn1 nanoclusters, we analyzed Homer1(+) synapses as a function of days in culture (days

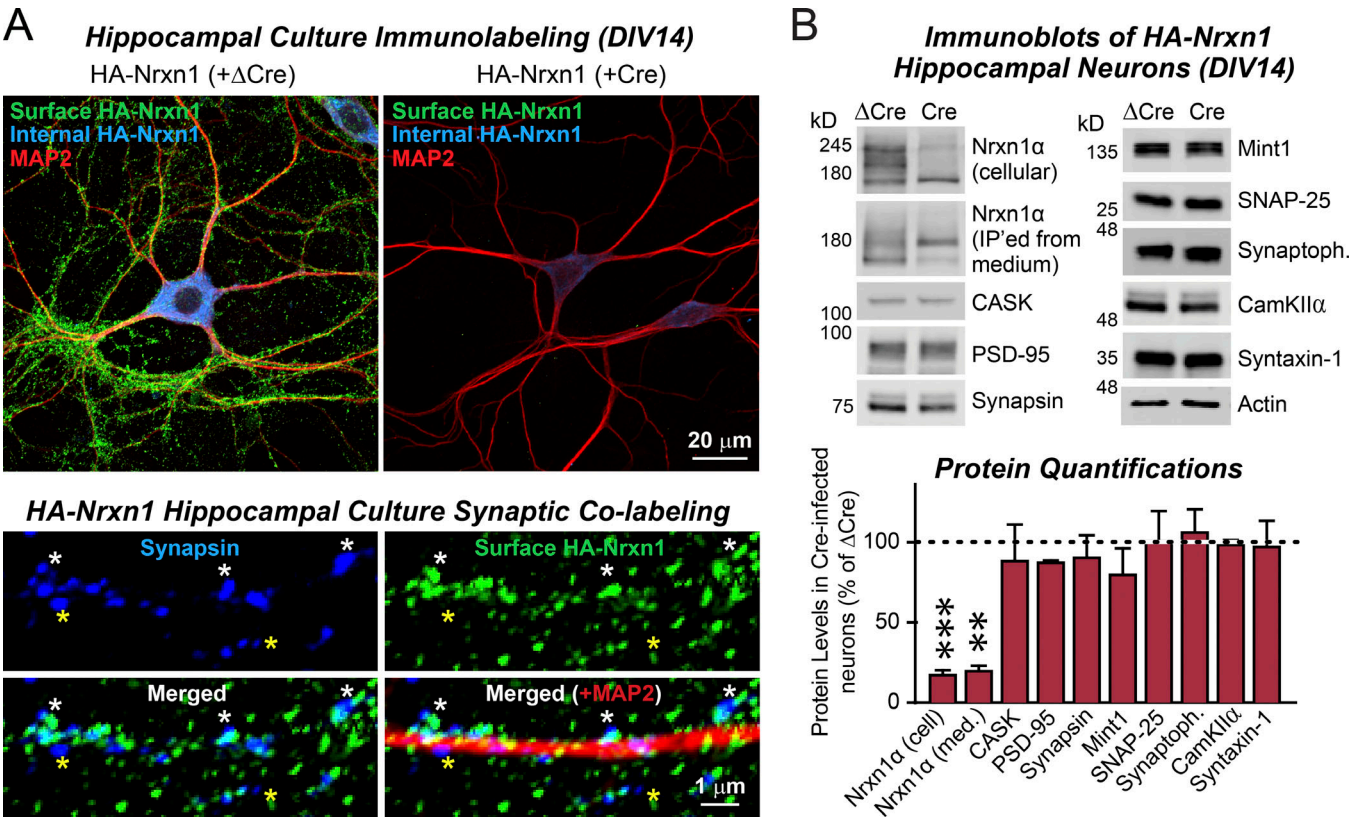

Figure 2. ***Nrxn1* cKI mice express full-length HA-tagged Nrxn1 in the absence of Cre recombination, but truncated HA-tagged Nrxn1 after Cre recombination. (A)** HA-tagged Nrxn1 exhibits a punctate surface-staining pattern in cultured hippocampal neurons. Representative images of HA-Nrxn1 cKI neurons expressing ΔCre (control, left) or Cre (to conditionally truncate HA-Nrxn1, right), and stained at DIV14 for surface-exposed and internal HA-Nrxn1 as well as for MAP2 (top, overview; bottom, zoomed-in to showcase synapses). White and yellow asterisks indicate synapsin puncta that do or do not colocalize with HA-Nrxn1 puncta, respectively. **(B)** Immunoblot analysis of proteins from hippocampal neurons treated as described in A reveals HA-Nrxn1 truncation but normal expression of selected synaptic proteins (top, representative blots; bottom, summary graph of protein levels). Data are means ± SEM; statistical significance was determined by one sample *t* test (**, $P < 0.01$; ***, $P < 0.001$; $n = 3$ cultures). For further details, see Fig. S1.

in vitro [DIV] 3–26) or postnatal (P) life (P1–28). Generally, we found that Nrxn1 nanoclusters grow in size and content during synapse maturation and slightly shift toward the periphery of the synapse (Fig. 4, A and E). In immature neurons (less than DIV5) and in mice younger than P10, <20% of Homer1(+) synapses contained Nrxn1 nanoclusters (Fig. 4, B and F). In more mature cultured neurons, the percentage of synapses with Nrxn1 nanoclusters more than doubled, leveling off at ∼40% of synapses by DIV10 (Fig. 4 B). In hippocampal tissue, however, the percentage of synapses with Nrxn1 nanoclusters continued to increase with age, reaching ∼40% of synapses at P28 (Fig. 4 F).

Both the Nrxn1 content per nanocluster and the relative size of the nanoclusters increased substantially during neuronal maturation in cultured neurons (Fig. 4, C and D; and Fig. S1 P) and in hippocampal tissue (Fig. 4, G and H). By comparison, the levels of Homer1 per synapse and the size of Homer1 discs did not increase substantially during synapse maturation in cultured neurons (Fig. S1, K and L) and showed a major increase only at P28 in vivo (Fig. S1, Q and R). Since Nrxn1 is also found at inhibitory synapses and extrasynaptic sites (Fig. 2 and Fig. S1 E), we quantified all Nrxn1 localizations not associated with Homer1 and found that maturation leads to increased Nrxn1 levels at sites other than Homer1(+) excitatory synapses (Fig. S1, M and S).

Finally, we measured the radial position of synaptic Nrxn1 nanoclusters relative to the synaptic cleft. We calculated both an absolute radial distance and a normalized distance to account for variation in synapse size. We found that Nrxn1 nanoclusters were generally located closer to the center of the synapse during early stages of development in cultured neurons and tissue, but moved slightly peripherally at later stages (Fig. S1, N, O, T, and U). Taken together, our data indicate that synaptic Nrxn1 nanoclusters substantially increase in abundance, size, and content as a function of development and synapse maturation.

Synaptic Nrxn1 nanoclusters are formed independent of HA-epitope tagging and include other neurexin isoforms

The observation of synaptic Nrxn1 nanoclusters was unexpected, as it suggests that synapses contain a hitherto unknown structural organization with a central neurexin pivot. However, our experimental approach may raise concerns about possible artifacts caused by the use of multivalent antibodies, the placement of the HA tag and loxP sequence, or the fixation method used. The discovery of Nrxn1 nanoclusters also raises an important question: Are Nrxn1 nanoclusters specific for Nrxn1, or do they contain other neurexins?

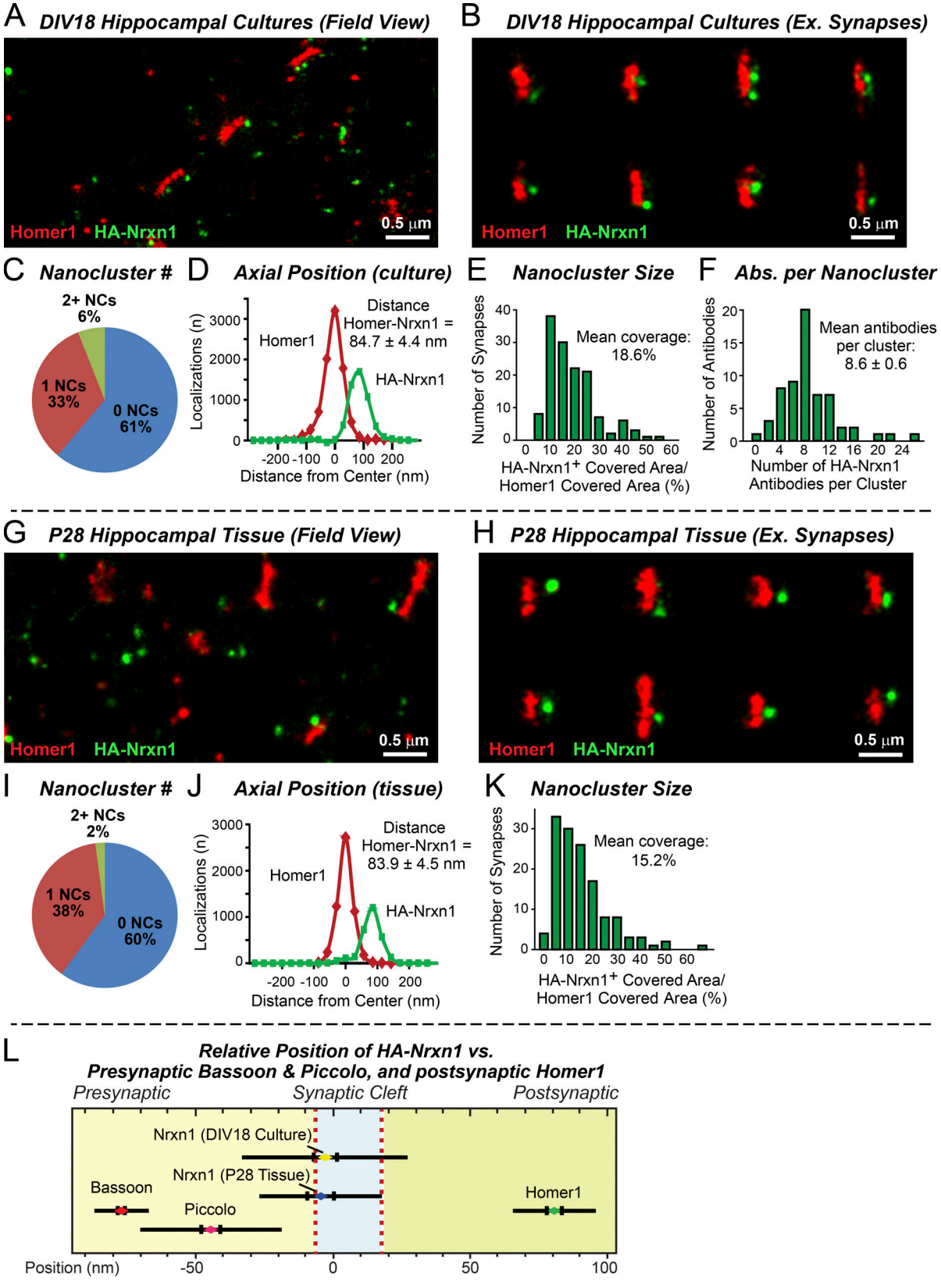

Figure 3. **Super-resolution STORM imaging identifies synaptic Nrxn1 nanoclusters. (A)** Representative image of cultured neurons at DIV18, showing multiple Homer1(+) synapses with a subset containing Nrxn1 nanoclusters. **(B)** Representative images of individual synapses from DIV18 neurons showing Homer1(+) synaptic junctions containing Nrxn1 nanoclusters. **(C)** Only a subset of Homer1(+) synapses contains Nrxn1 nanoclusters (NCs; 39%) in cultured neurons at DIV18. **(D)** Homer1 discs and Nrxn1 nanoclusters are separated by ∼85 nm across the synapse. The trans-axial distribution of Homer1 and HA-Nrxn1 localizations was determined by STORM imaging of hippocampal cultures at DIV18. **(E)** Nrxn1 nanoclusters occupy on average ∼19% area of the Homer1-

defined synaptic junction. **(F)** Nrxn1 nanoclusters are on average labeled by approximately nine antibodies per nanocluster. **(G–K)** Same as A–E, except that cryostat sections of the hippocampal CA1 region from HA-Nrxn1 cKI mice were analyzed at P28. **(L)** Quantification of the axial distribution of STORM localizations of surface HA-Nrxn1 in hippocampal neurons or cryosections relative to those of Homer1, Piccolo, and Bassoon. Short vertical bars = SEMs; horizontal bars = SDs. For C–F, *n* = 54 synapses/three cultures; for I–K, *n* = 77 synapses/three mice. For further details, see Fig. S1.

To address these questions, we first tested whether the Nrxn1 nanoclusters are caused by antibody-induced aggregation during live-cell labeling. We compared Nrxn1 nanoclusters in cultured neurons live-labeled with HA antibody or stained after light and harsh chemical fixation, but observed no major differences (Fig. S2, A–J). Thus, the Nrxn1 nanoclusters are unlikely to be artifacts caused by live antibody labeling or fixation.

Next, we examined whether the formation of the nanoclusters was a native property of neurexins that is independent of the HA-tagging and also includes other neurexins. We used a pan-neurexin antibody that recognizes the conserved C-terminus of Nrxn1 and reacts with all neurexins and that was previously employed for immuno-EM analyses (Pregno et al., 2013). Hippocampal neurons from Nrxn1 conditional knockout (cKO) mice (Chen et al., 2017) expressing ΔCre or Cre were labeled with the pan-neurexin antibody. We observed in the control neurons (ΔCre) the same synaptic nanoclusters we had detected using HA antibody in HA-Nrxn1 cKI neurons and found no difference in homer levels (Fig. 5, A–D; and Fig. S2, K–N).

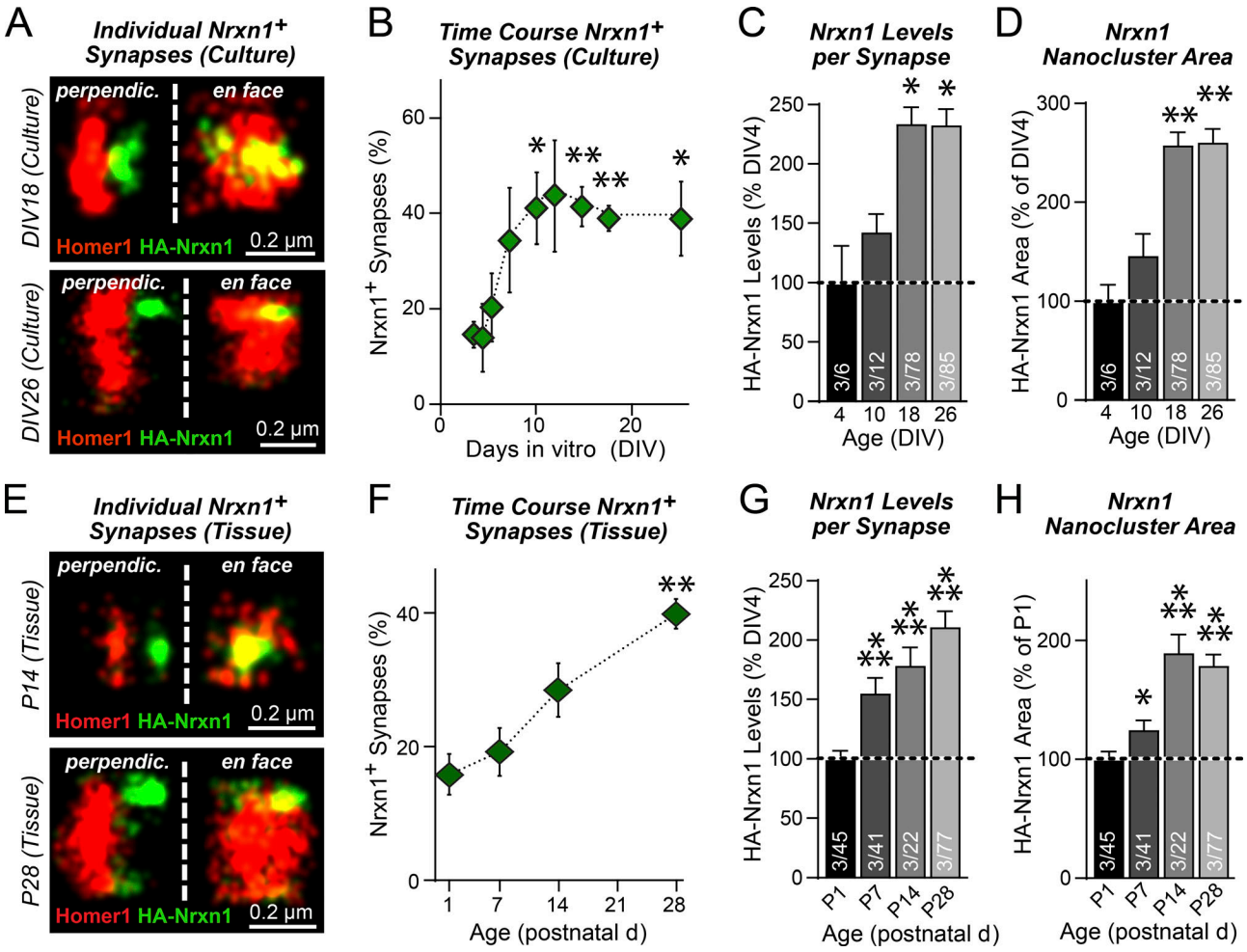

Figure 4. **Synaptic Nrxn1 nanoclusters are dynamic across development. (A)** Example synapses illustrating the features of Nrxn1 nanoclusters in cultured neurons at DIV18 (top) and DIV26 (bottom), including central and peripheral localizations of Nrxn1 nanoclusters (scale bars, 0.2 µm). **(B)** The percentage of Homer1(+) synapses with Nrxn1 nanoclusters in cultured neurons as a function of culture time. **(C and D)** The relative Nrxn1 content (C) and size of synaptic Nrxn1 nanoclusters (D) increase during development in hippocampal neurons analyzed at the indicated culture DIVs (shown as percentage of DIV4 levels). **(E)** Same as A, except of Nrxn1 nanoclusters in hippocampal CA1 region from HA-Nrxn1 cKI mice at P14 (top) and P28 (bottom; scale bars, 0.2 µm). **(F)** Same as B, except that cryostat sections of the hippocampal CA1 region from HA-Nrxn1 cKI mice were analyzed as a function of age. **(G and H)** Same as C and D, but for cryostat sections of the hippocampal CA1 region of HA-Nrxn1 cKI mice analyzed at P1–28 (values are expressed as percentage of P1). Numerical data are means ± SEM. Statistical significance was determined by two-sample *t* test to earliest time point (*, $P < 0.05$; **, $P < 0.01$; ***, $P < 0.001$). For B and F, *n* = 3 cultures or mice, averaged per culture or mouse; for C and D, *n* as number of synapses = 6, DIV4; 12, DIV10; 78, DIV18; 85, DIV26/three cultures; for G and H, *n* as number of synapses = 45, P1; 41, P7; 22, P14; 77, P28/three mice. For further details, see Fig. S1.

Notably, the pan-neurexin antibody still recognized Nrxn nanoclusters in Nrxn1 cKO neurons (Fig. 5, A–D) and in HA-Nrxn1 cKI neurons (Fig. S2, Q–U) after expression of Cre-recombinase, whereas under the same conditions, HA antibodies no longer detected the nanoclusters (Fig. S1 H). However, we did not detect Nrxn nanoclusters in neurons cultured from Nrxn123 triple cKO mice (Chen et al., 2017) following expression of Cre (Fig. 5, E–H), confirming the specificity of the pan-neurexin antibody. No change in Homer1 levels or area was detected following Cre expression (Fig. S2, O and P). Thus, Nrxn2 and Nrxn3 are likely present in the synaptic nanoclusters even in the absence of Nrxn1. Direct comparison of Nrxn1 nanoclusters observed using HA antibodies in HA-Nrxn1 cKI neurons with neurexin nanoclusters observed using pan-neurexin antibodies in control neurons revealed that these nanoclusters had similar properties (Fig. S2, V–Z). Thus, Nrxn1 nanoclusters are independent of the HA tag and contain other neurexins in addition to Nrxn1.

To confirm that pan-neurexin and HA antibodies recognize the same nanoclusters, we labeled hippocampal neurons from HA-Nrxn1 cKI mice with pan-neurexin and HA antibodies for two-color STORM imaging, and with Homer1 antibody for conventional wide-field microscopy (Fig. 5 I). We then measured the pan-neurexin signal at Homer1(+) synapses containing or lacking HA-Nrxn1 nanoclusters. We found that nearly all synapses containing HA-Nrxn1 nanocluster(s) also featured pan-neurexin nanocluster(s) (Fig. 5, J and L), and that nearly all synapses containing a pan-neurexin nanocluster(s) also featured a HA-Nrxn1 nanocluster(s) (Fig. 5, K and M). Moreover, the HA-Nrxn1 and pan-neurexin clusters exhibited a high degree of colocalization (~80% volume overlap; Fig. 5 N). Taken together, these findings confirm that HA and pan-neurexin antibodies recognize the same nanoclusters, which include Nrxn1 as well as other neurexin isoforms.

Functional differences in synapses containing Nrxn1 clusters

What is the function of neurexin nanoclusters? Addressing this question is currently difficult, since there are no known neurexin mutants that selectively interfere with nanoclustering while preserving synaptic targeting. Extensive studies of Nrxn1 function using genetic manipulations in vivo followed by slice physiology have revealed that Nrxn1 has an important role in shaping synaptic properties, but not in the basic processes of synapse formation and synaptic transmission (Etherton et al., 2009; Dai et al., 2019). Using hippocampal neurons cultured from Nrxn1 cKI and cKO mice, we found that Nrxn1 is not essential for excitatory synapse formation or maintenance (Fig. S3, A–I and P–S). We also found no change in basic properties of synaptic transmission, including in spontaneous AMPA receptor currents (Fig. S3, J–O and T–Y).

Another approach for ascertaining the function of neurexin nanoclusters is to compare the properties of synapses that contain or lack nanoclusters. We found that Homer1 levels were similar in synapses containing or lacking Nrxn1 or pan-neurexin nanoclusters (Fig. 6, A–F), suggesting that the overall size of synapses does not vary based on the presence of nanoclusters. We next asked whether nanoclusters were preferentially associated with active synapses. Since neurexin nanoclusters can only be identified using STORM, functional properties must be inferred optically. We used two optical approaches for these experiments, measurements of the relative amounts of postsynaptic surface GluA1 AMPA receptors (Aoto et al., 2013), and assessment of presynaptic vesicle exocytosis by live labeling of neurons with antibodies to the luminal domain of synaptotagmin-1 (Syt1) that becomes exposed during synaptic vesicle exocytosis (Kraszewski et al., 1995). We observed that synapses containing Nrxn1 nanoclusters exhibited significantly more surface GluA1 receptors than synapses lacking Nrxn1 nanoclusters (Fig. 6, G–I), and displayed much higher levels of synaptic vesicle exocytosis (Fig. 6, J–L). These results suggest that excitatory synapses possessing Nrxn1 nanoclusters are functionally more active than those that do not. These observations do not contradict our observation that conditional deletion of Nrxn1 had no effect on synapse density and activity for the following reasons: (1) Nrxn2 and Nrxn3 substitution at nanoclusters may compensate for the absence of Nrxn1, and (2) the function of Nrxn1 in cultured neurons may relate to additional synaptic properties not measured here, such as postsynaptic N-methyl-D-arginine receptor–mediated responses (Dai et al., 2019).

The fact that Nrxn1 nanoclusters are enriched in active synapses prompted us to ask whether synaptic activity regulates Nrxn1 nanoclusters. We found that Nrxn1 content, percentage of excitatory synapses with Nrxn1 nanoclusters, and the amount of Homer1 at excitatory synapses were not significantly influenced by manipulations of synaptic activity in mature (Fig. S4, A–H) and developing cultured neurons (Fig. S4, I–P). Instead, in a manner similar to what occurs during synapse maturation (Fig. S1, N, O, T, and U), increasing activity via synaptic disinhibition shifted HA-Nrxn1 nanoclusters from the center of the active zone toward the periphery in both developing and mature cultures (Fig. S4, E, F, M, and N). Thus, although Nrxn1 nanoclusters are a marker of active synapses, their abundance is not controlled by synaptic activity.

Dynamics of Nrxn1 expression and processing

Cultured neurons release Nrxn1 fragments into the medium, suggesting that Nrxn1 is physiologically processed by ectodomain cleavage (Fig. 2 B). Does Nrxn1 ectodomain cleavage occur at a physiologically relevant rate? To begin to address this question, we examined secretion of Nrxn1 ectodomains in hippocampal neurons cultured from HA-Nrxn1 cKI mice (Fig. 7 A). Direct comparison of Nrxn1α proteins in the cell lysates and medium from neurons expressing ΔCre or Cre-recombinase showed that without Cre recombination, neurons release a Nrxn1α fragment into the medium that contains the HA-epitope and is ~20 kD smaller than full-length Nrxn1α in cell lysates, suggesting that Nrxn1α is subject to site-specific proteolysis in the sequence separating the HA-epitope from the membrane (Fig. 7 B). We measured the relative amount of ectodomain cleavage in hippocampal, cortical, and olfactory bulb neurons as a function of culture time (Fig. 7 C). Although hippocampal, cortical, and olfactory bulb neurons exhibited different Nrxn1α expression levels, they released comparable amounts of Nrxn1α

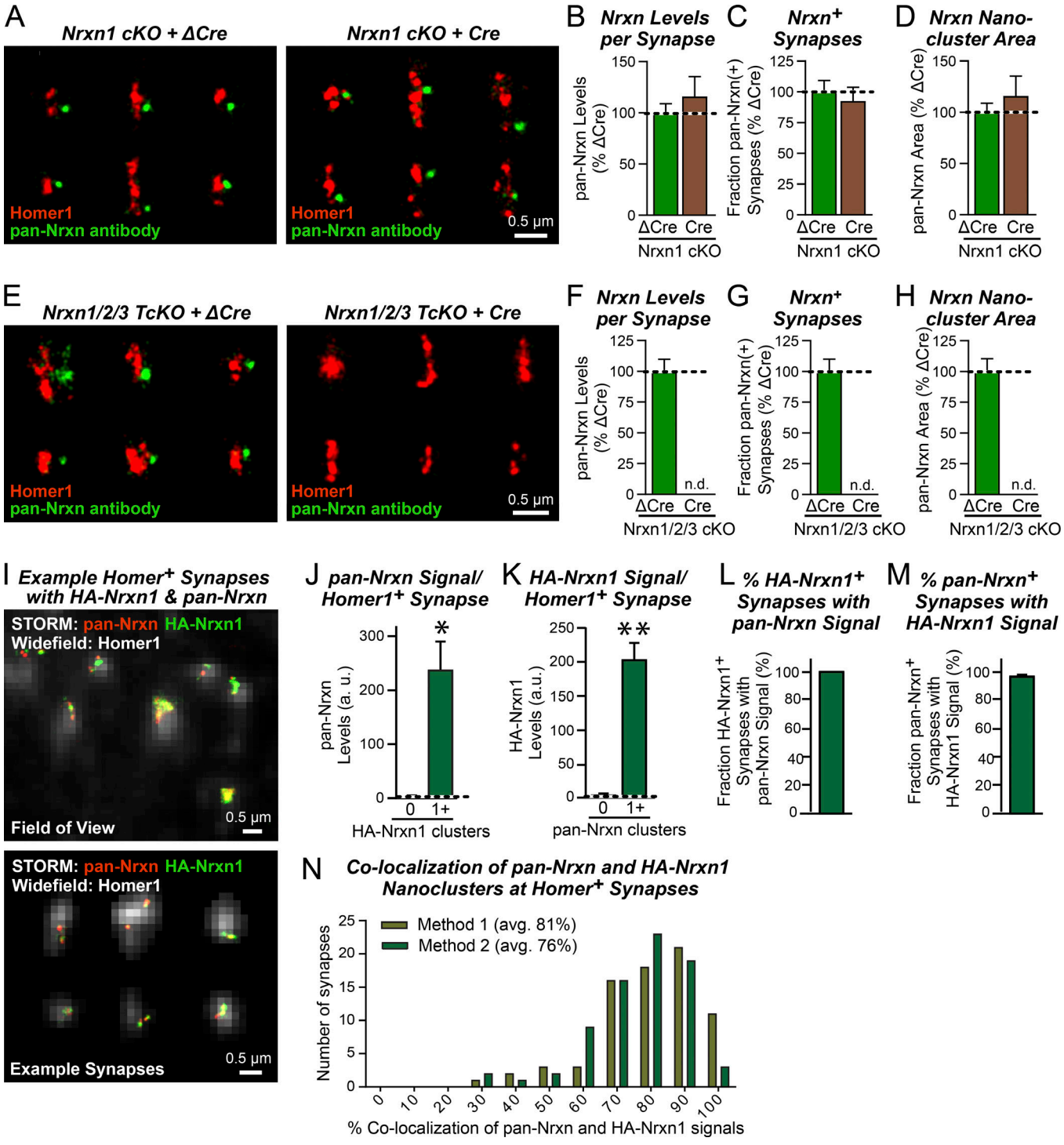

Figure 5. **Synaptic Nrxn1 nanoclusters are independent of HA-epitope tagging and contain other neurexins. (A)** Labeling with a pan-neurexin antibody shows neurexin nanoclusters in DIV12 hippocampal neurons from Nrxn1 cKO mice that are not abolished following Cre expression (scale bar, 0.5 µm). **(B–D)** Neurexin content per nanocluster (B), proportion of neurexin(+) synapses (C), and area occupied by a nanocluster (D) are indistinguishable in Nrxn1 cKO mice expressing ΔCre or Cre. **(E)** Expression of Cre in hippocampal cultures (DIV12) from Nrxn1/2/3 triple cKO mice abolishes nanoclusters labeled with a pan-neurexin antibody (scale bar, 0.5 µm). **(F–H)** Pan-deletion of all neurexins abolishes neurexin content per nanocluster (F), proportion of neurexin(+) synapses (G), and area occupied by a nanocluster (H); n.d. indicates not detectable. **(I)** Representative field of view (top) and a subset of exemplary Homer1(+) synapses (bottom) containing HA-Nrxn1 (detected by anti-HA) and total neurexins (detected by pan-neurexin antibody) imaged using STORM. The Homer1 signal is imaged using conventional wide-field microscopy (scale bars, 0.5 µm). **(J)** Synaptic pan-Neurexin content of Homer1(+) synapses having one or more HA-Nrxn1 clusters compared with those without clusters. **(K)** Synaptic HA-Nrxn1 content of Homer1(+) synapses having one or more pan-Nrxn1 clusters compared with those without clusters. **(L and M)** Fraction of HA-Nrxn1(+) (L) or pan-Nrxn(+) (M) synapses also containing pan-Nrxn and HA-Nrxn1 signal, respectively. **(N)** Co-localization between neurexin nanoclusters defined by pan-Nrxn and HA-Nrxn1 using the coarse convex hull method (method 1) or convex hull method (method 2). Numerical data are means ± SEM. Statistical significance was determined by two-sample *t* test to ΔCre or synapses having 0 HA-Nrxn1 clusters (*, $P < 0.05$; **, $P < 0.01$). For B–D, *n* as number of synapses = 17, ΔCre; 9, Cre/three cultures; for F–H, *n* as number of synapses = 18, ΔCre; 14, Cre/three cultures; for J–M, *n* = 3 cultures; for N, *n* = 75 synapses). For further details, see Fig. S2.

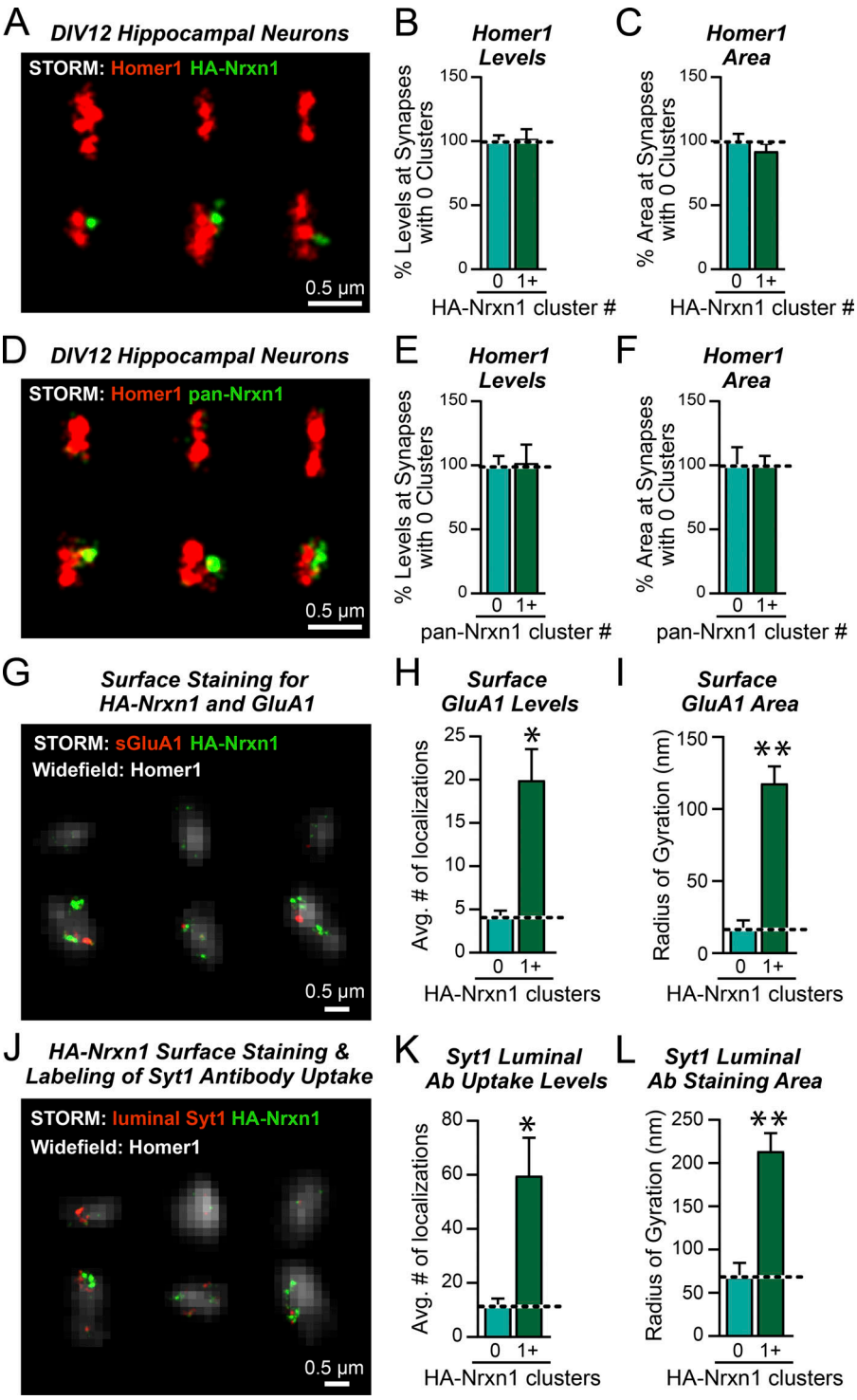

Figure 6. **Excitatory synapses containing Nrxn1 nanoclusters exhibit higher surface GluA1 levels and more active presynaptic vesicle exocytosis. (A)** Representative synapses from HA-Nrxn1 cKI hippocampal neurons (DIV12) showing synapses without (top row) and with (bottom row) Nrxn1 nanoclusters (scale bar, 0.5 µm). **(B and C)** Homer1 levels (B) and area (C) are indistinguishable at synapses having 0 or 1+ Nrxn1 nanoclusters. **(D)** Representative images of individual synapses from WT hippocampal neurons (DIVI2) showing synapses without (top row) and with (bottom row) pan-neurexin nanoclusters (scale bar, 0.5 µm). **(E and F)** Homer1 levels (E) and area (F) are indistinguishable at synapses having 0 or 1+ pan-neurexin nanoclusters. **(G)** Homer1(+) synapses containing Nrxn1 nanoclusters have higher levels of surface AMPA receptor subunit 1 (sGluA1; bottom row) than synapses without nanoclusters (top row; scale bar, 0.5 µm). **(H and I)** Surface GluA1 content (H) and area (I) are higher at Homer1(+) synapses containing one or more HA-Nrxn1 clusters relative to synapses without HA-Nrxn1 nanoclusters. **(J)** Homer1(+) synapses containing Nrxn1 nanoclusters have higher levels of presynaptic vesicle exocytosis visualized following uptake of an antibody recognizing the luminal domain of synaptotagmin-1 (Syt1; scale bar, 0.5 µm). **(K and L)** Luminal Syt1 antibody uptake levels (K) and area (L) are higher at Homer1(+) synapses containing one or more Nrxn1 nanoclusters relative to those that do not contain Nrxn1 nanoclusters. Numerical data are means ± SEM. Statistical significance was determined by a two-sample *t* test to neurexin cluster # = 0 (*, $P < 0.05$; **, $P < 0.01$). For B and C, *n* as number of synapses = 27, 0 nanoclusters; 20, 1+ nanoclusters/three cultures; for E and F, *n* as number of synapses = 24, 0 nanoclusters; 16, 1+ nanoclusters/three cultures; for H and I and K and L, *n* = 3 cultures.

fragments into the medium (Fig. 7, D and E). Surprisingly, Nrxn1 cleavage was not dependent on synaptic activity (Fig. S4, Q–S).

A potential concern of the experiments probing Nrxn1 ectodomain cleavage in cultured neurons is that neuronal cultures include activated astrocytes and microglia that may promote proteolysis of cell surface proteins. To address this concern, we examined the relative amount of the released soluble Nrxn1α fragment in mouse brain. We fractionated total brain homogenates from HA-Nrxn1 cKI mice and from WT control mice into a membranous pellet and a soluble supernatant, and analyzed these fractions by immunoblotting with a series of antibodies (Fig. 8 A). These analyses showed that the protein levels in the fractions from HA-Nrxn1 cKI and WT mice were similar overall, ruling out major changes induced in brain composition by the HA-Nrxn1 cKI (Fig. 8, B and C).

Next, we quantified the relative amounts of ectodomain-cleaved vs. membrane-associated Nrxn1α in adult brain at P56 using the fractionation scheme outlined above. In these

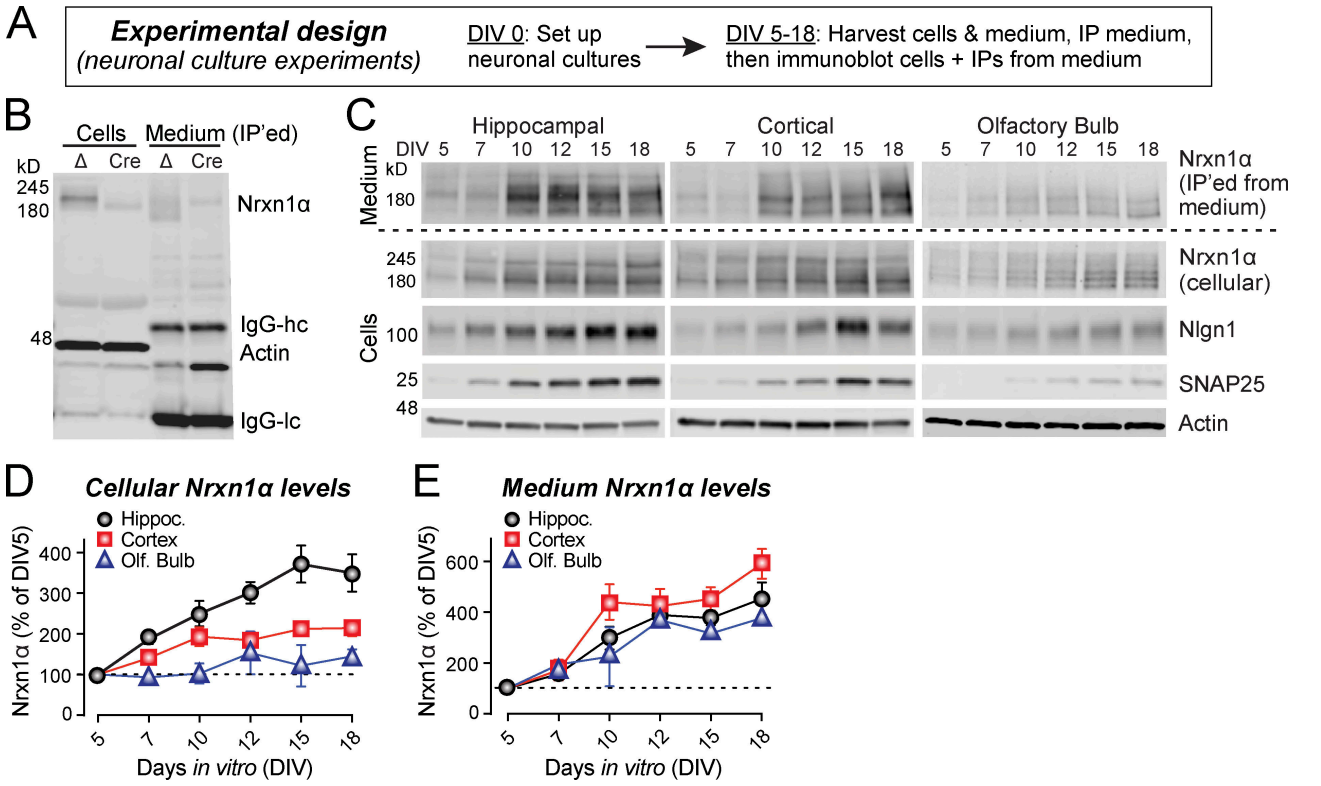

Figure 7. **Nrxn1 is extensively cleaved across synaptic development in cultured neurons. (A)** Cultured hippocampal neurons from HA-Nrxn1 cKI mice for defined DIV5–18 were analyzed by quantitative immunoblotting directly (cell lysates) or after immunoprecipitation with HA antibodies (medium). **(B)** Immunoblotting shows HA-Nrxn1α in cell lysates and in the medium of HA-Nrxn1 neurons expressing ΔCre, but detects only a faint amount of HA-Nrxn1α in either sample after Cre-mediated truncation of Nrxn1. **(C)** Levels of cellular and cleaved Nrxn1α rise in parallel with culture time. Images show representative immunoblots of hippocampal, cortical, and olfactory bulb neurons cultured from HA-Nrxn1 cKI mice and analyzed at DIV5, 7, 10 12, 15, and 18. **(D and E)** The levels of cellular Nrxn1α and of Nrxn1α released by proteolysis into the medium increase coordinately with culture time. Summary plots depict protein levels determined by quantitative immunoblotting in the cells (D) and medium (E, monitored after immunoprecipitation) as a function of culture time. Data are means ± SEM (n = 5, hippocampal; 6, cortical; 2, olfactory bulb cultures).

experiments, we also examined the levels of ectodomain-cleaved vs. membrane-associated neuroligin-1 (Nlgn1), a neurexin ligand that was previously shown to be proteolytically processed (Peixoto et al., 2012; Suzuki et al., 2012). We observed the highest levels of Nrxn1α ectodomain cleavage in cortex and hippocampus, in which soluble Nrxn1α proteins represented ∼6% of the total full-length Nrxn1α (Fig. 8, D and E). Nrxn1α ectodomain cleavage in the cerebellum was significantly lower than in other regions, suggesting that the tissue context of Nrxn1 expression may control ectodomain cleavage (Fig. 8, D and E). Importantly, the relative Nlgn1 ectodomain concentration was twofold lower than that of the Nrxn1α ectodomain, suggesting that Nrxn1α ectodomain cleavage exceeds Nlgn1 cleavage (Fig. 8, D and E).

Nrxn1 ectodomain cleavage is largely mediated by ADAM10

To determine what proteases are responsible for Nrxn1 ectodomain cleavage, we first surveyed ectodomain protease inhibitors for their ability to decrease Nrxn1 cleavage cultured neurons from HA-Nrxn1 cKI mice (Fig. 9, A and B). After application of various inhibitors at DIV10 for 48 h, we found that inhibitors of matrix metalloproteases (MMPs) in general (GM6001) or ADAM-type sheddases in particular (TAPI-2) suppressed the release of the cleaved Nrxn1 fragment into the medium by ∼60% in hippocampal and cortical neurons (Fig. 9, C–H). Because ADAM10 is a major ectodomain metalloprotease in brain that has been suggested to cleave Nlgn1 (Peixoto et al., 2012; Saftig and Lichtenthaler, 2015; Kuhn et al., 2016), we tested more specific ADAM10/17 and ADAM10 inhibitors (GW280264X or GI254023X, respectively). In hippocampal neurons, we found that the ADAM10-specific inhibitor was as effective as the broad-spectrum metalloprotease inhibitors and the ADAM10/17 inhibitor in blocking Nrxn1 ectodomain cleavage, but was less effective in cortical neurons, indicating that ADAM10/17 activity may differ between brain regions (Fig. 9, C–H). Blocking MMP9 (SB-3CT), which has been implicated in synaptic function and reported to mediate Nlgn1 cleavage (Peixoto et al., 2012; Murase et al., 2017), had no effect on Nrxn1 ectodomain cleavage (Fig. 9, C–H). Similarly, blocking BACE1 (C3), another abundant ectodomain protease in the brain, did not significantly affect Nrxn1 ectodomain cleavage (Fig. 9, C–H). These data suggest that Nrxn1 ectodomain cleavage is primarily mediated by ADAM10. This conclusion is further supported by our findings that both a partial knockdown of ADAM10 and overexpression of a dominant-negative ADAM10 mutant decrease ectodomain cleavage of Nrxn1 (Fig. S5, A–F).

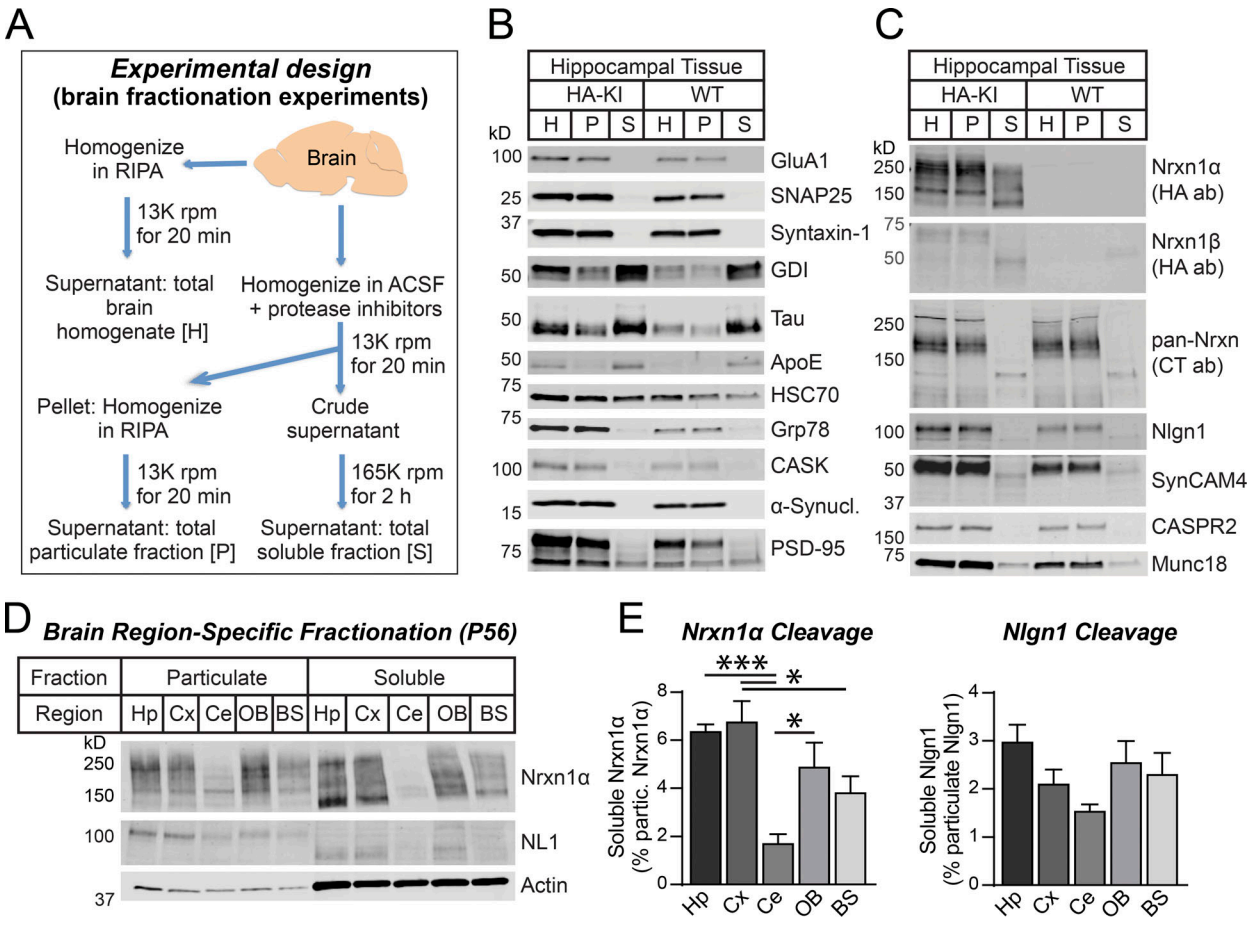

Figure 8. **Nrxn1 is cleaved physiologically by proteolysis at approximately twice the rate of neuroligin-1. (A)** Brain subcellular fractionation protocol to obtain the total homogenate (H) and to separate soluble proteins (S) from membrane-associated proteins in the particulate fraction (P). **(B)** Validation of subcellular fractions isolated from the hippocampus of adult HA-Nrxn1 cKI (left) and WT mice (right) at P56. Lanes were loaded with equivalent amounts of H and P fractions, but 10 times more of the S fraction. **(C)** Nrxn1α and Nrxn1β are both detected in particulate and soluble brain fractions. Note that soluble Nrxn1α and Nrxn1β proteins are smaller than cellular Nrxn1α and Nrxn1β, as would be expected for fragments released by proteolytic cleavage. Note also that the HA antibody only detects HA-Nrxn1 from cKI mice, whereas the pan-neurexin antibody detects Nrxn1 in both Nrxn1 cKI and in WT brain lysates. **(D and E)** Soluble Nrxn1α fragments are produced in all brain regions, and are present at approximately twice the levels of soluble Nlgn1 fragments. Summary graphs show the amount of soluble Nrxn1α (left) and Nlgn1 (right) as percent of the total as determined by quantitative immunoblotting in subcellular fractions from the indicated brain regions of HA-Nrxn1 cKI mice analyzed at P56 (Hp, hippocampus; Cx, cortex; Ce, cerebellum; OB, olfactory bulb; BS, brain stem). Lanes were loaded with equivalent amounts of H and P fractions, but 20 times more of the S fraction. Data are means ± SEM; statistical significance was determined by a one-way ANOVA and Tukey's post hoc test (*, $P < 0.05$; ***, $P < 0.001$; $n = 6$ mice for the Nrxn1α and 3 mice for the Nlgn1 quantification).

Blocking proteolytic Nrxn1 cleavage substantially enhances Nrxn1 nanoclusters

We next asked whether inhibition of Nrxn1 ectodomain cleavage alters synaptic Nrxn1 nanoclusters. We imaged synapses by STORM at DIV12 after a 48-h application of protease inhibitors (Fig. 10 A). Strikingly, protease inhibitors that impaired Nrxn1 ectodomain cleavage caused a large enhancement of synaptic Nrxn1 nanoclusters. Specifically, the broad-spectrum MMP inhibitor (GM6001) or protease inhibitors targeting ADAM10 (GW280264X or GI254023X) increased the percentage of synapses containing Nrxn1 nanoclusters almost twofold, enhanced the number of synapses with two or even three Nrxn1 nanoclusters, and augmented the Nrxn1 content of these nanoclusters (Fig. 10, B–D). The protease inhibitors additionally increased the physical size of synaptic Nrxn1 nanoclusters, although this effect was statistically significant only for the ADAM10 inhibitor GI254023X (Fig. 10 E). The inhibitors did not consistently affect the Homer1 content of synapses or the radial position of Nrxn1 nanoclusters (Fig. 10, F and G; and Fig. S5, G and H). In contrast to metalloprotease and ADAM10 inhibitors, β-secretase (BACE) inhibition had no effect on synaptic Nrxn1 nanoclusters (Fig. 10, A–G; and Fig. S5, G and H). The substantial increase in the content of Nrxn1 nanoclusters and the doubling of synapses associated with Nrxn1 nanoclusters observed following ADAM10 inhibition suggests that nanoclusters are dynamically regulated by ADAM10, and that all (or nearly all) synapses are capable of acquiring such nanoclusters. Inhibition of ADAM10 did not significantly alter excitatory synapse density (Fig. S5, J–R), suggesting that the increase in synapses associated with Nrxn1 nanoclusters following ADAM10 inhibition is not due to a selective loss of synapses lacking Nrxn1 nanoclusters. Moreover, the actions of ADAM10 on constraining surface Nrxn1 levels

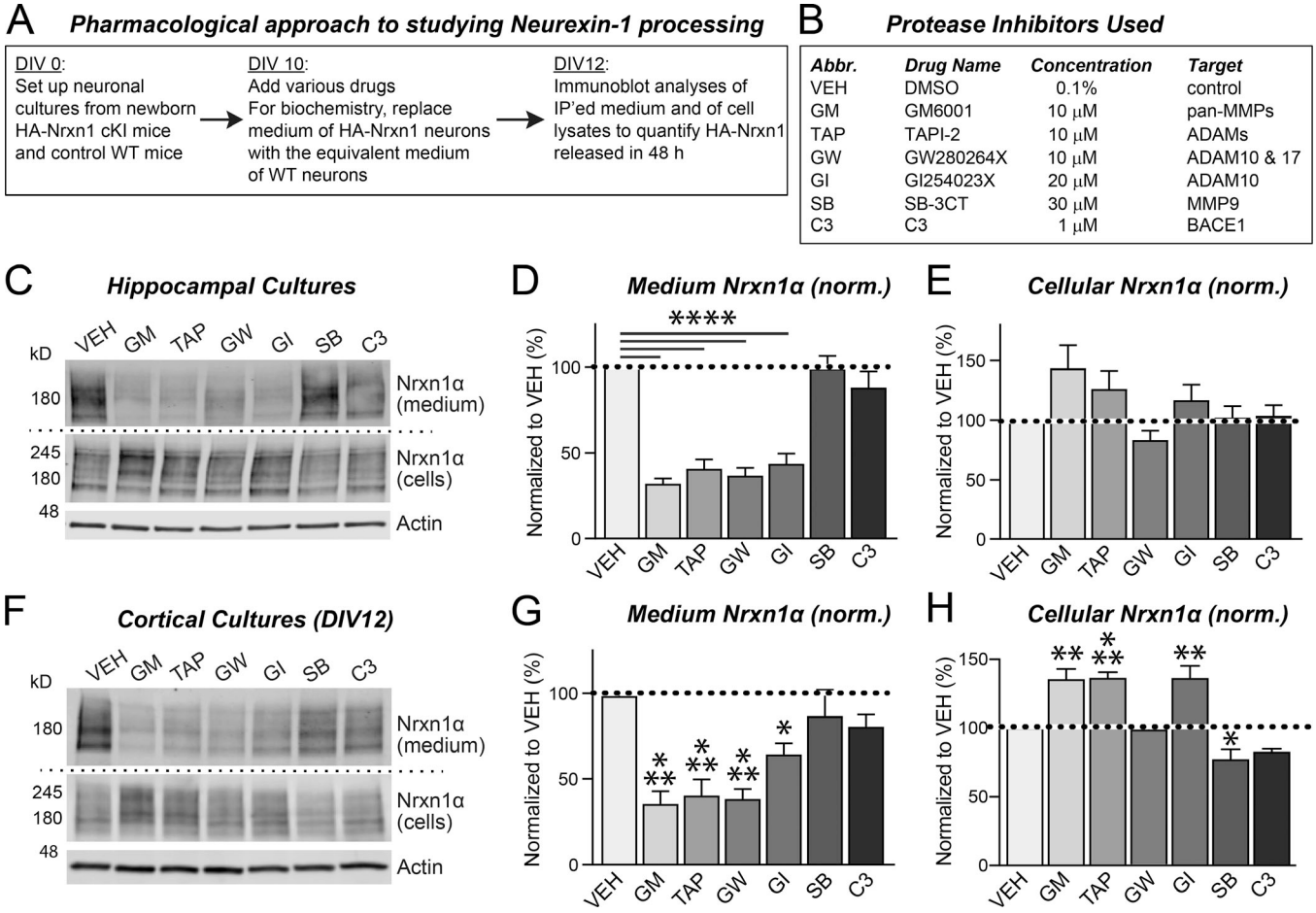

Figure 9. **ADAM10 is the major Nrxn1 sheddase in dissociated hippocampal and cortical cultures. (A)** Experimental design of metalloprotease inhibition experiments. **(B)** Protease inhibitors used for experiments. **(C)** Immunoblot analysis of the HA-Nrxn1α fragment released into the medium and of cellular HA-Nrxn1α in HA-Nrxn1 cKI hippocampal neurons and treated with the indicated protease inhibitors or vehicle control (VEH). See A and B for abbreviations and details. **(D and E)** Summary graphs of the levels of Nrxn1α fragments released in the medium (D) and of full-length Nrxn1α present in the cells (E) as a function of the treatment of hippocampal neurons with the indicated protease inhibitors, determined by quantitative immunoblotting of HA-Nrxn1 from HA-Nrxn1 cKI mice. **(F–H)** Same as C–E, except results are from cortical neurons. Data are means ± SEM. For D–H, statistical significance was determined by one-sample *t* test (*, $P < 0.05$; **, $P < 0.01$; ***, $P < 0.001$; ****, $P < 0.0001$). For D and E, *n* as number of cultures = for medium: 12, VEH; 12, GM; 12, TAP; 6, GW; 12, GI; 11, SB; 12, C3; for cellular: 9, VEH; 8, GM; 9, TAP; 5, GW; 8, GI; 9, SB; 9, C3; for F–H, *n* = 4 cultures for medium and cellular. For further details, see Fig. S5.

appear to be a major feature of excitatory synapses, since none of the MMP inhibitors significantly altered the levels of Nrxn1 not associated with Homer1(+) synapses (Fig. S5 I). Altogether, these results demonstrate that Nrxn1 nanoclusters likely exist in a steady-state of formation vs. destruction, partially or entirely.

Discussion

Here, we identify by super-resolution imaging a previously unknown nanoscale organization of excitatory synapses characterized by discrete neurexin nanoclusters. We found that Nrxn1 is coassembled with other neurexins in the synaptic cleft into nanoclusters, with a given Nrxn1(+) synapse generally containing only a single Nrxn1 nanocluster that is on average comprised of at least four Nrxn1 molecules and that is dynamically regulated by ectodomain cleavage but not by synaptic activity. Thus, the spatial distribution of Nrxn1 is similar neither to the proposed nanocolumns that align the presynaptic release machinery with postsynaptic receptors (Tang et al., 2016; Biederer et al., 2017; Chen et al., 2018; Hruska et al., 2018), nor to the perisynaptic localization displayed by N-cadherin or SynCAM (Uchida et al., 1996; Perez de Arce et al., 2015). Given that neurexins function in regulating synapse properties (Südhof, 2017), the Nrxn1 nanoclusters identified here may serve as pivots for the synapse-organizing functions of neurexins. In support of this hypothesis, we found that synapses containing Nrxn1 nanoclusters exhibit higher levels of postsynaptic GluA1 receptors and a greater rate of presynaptic vesicle exocytosis than synapses lacking Nrxn1 nanoclusters. In contrast to the Nrxn1 nanoclusters, the pre- and postsynaptic proteins that are aligned in nanocolumns were proposed to coordinate neurotransmitter release and reception (Biederer et al., 2017), as recently revealed by localization of AMPA receptor nanocolumns as a function of long-term plasticity (Hruska et al., 2018). Thus, the distinct structural organizations of Nrxn1 nanoclusters and repeated nanocolumns are consistent with the difference in their proposed roles in synaptic function.

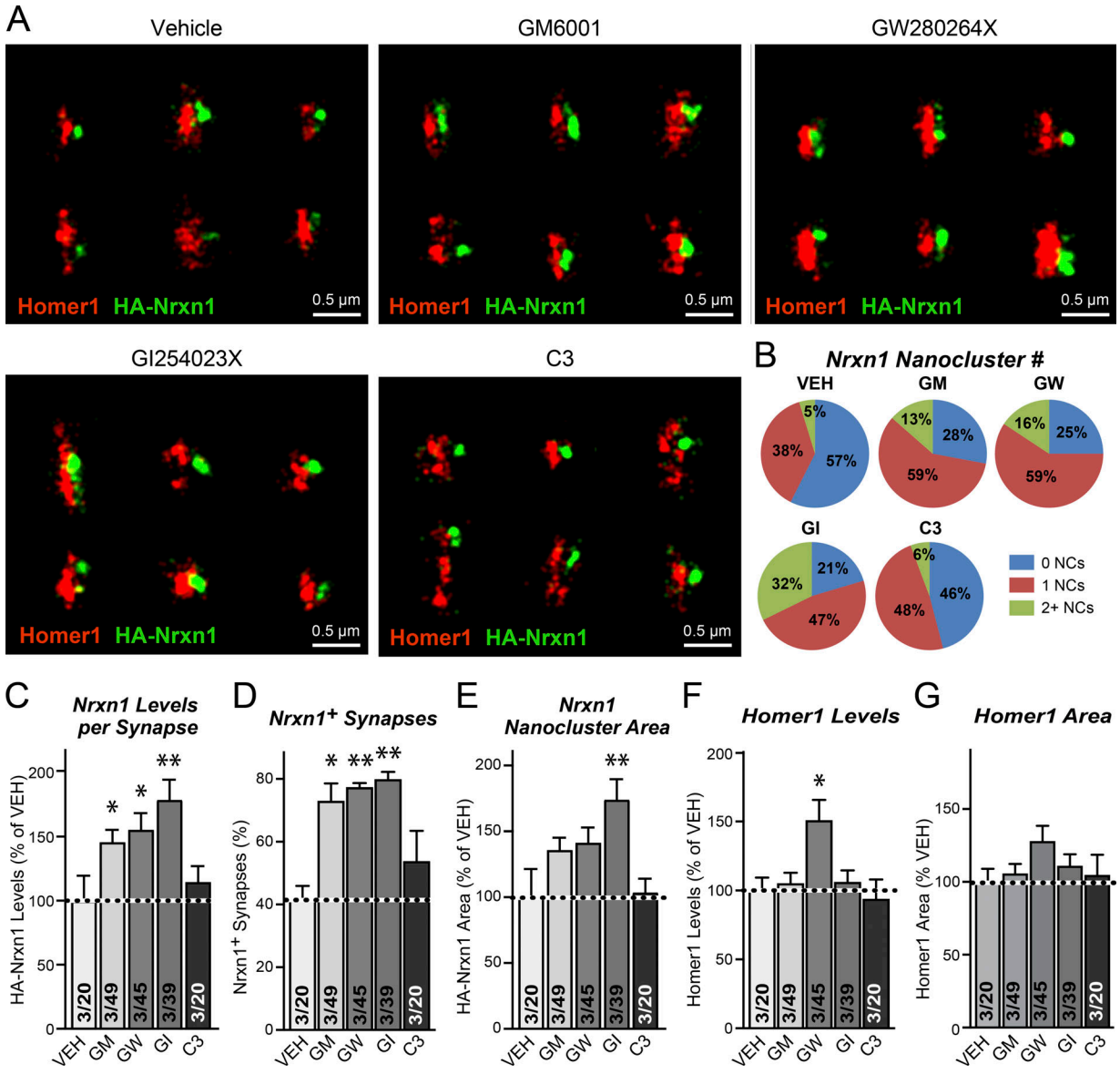

Figure 10. **ADAM10 inhibition dramatically enhances Nrxn1 nanocluster presence and content at excitatory synapses. (A)** Representative 3D STORM images of Homer1(+) synapses with surface HA-Nrxn1 clusters visualized in hippocampal neurons treated with the indicated protease inhibitors from DIV10-12 (scale bars, 0.5 µm). Drugs are detailed in Fig. 9 B. **(B)** Pie charts of the number of nanoclusters per Nrxn1(+) synapse show that MMP/ADAM10 blockage increases the proportion of synapses containing Nrxn1 nanoclusters. **(C–G)** Summary graphs showing that ADAM10 inhibition substantially increases the content of Nrxn1 nanoclusters (C) and the fraction of synapses containing Nrxn1 nanoclusters (C). The areas of Nrxn1 nanoclusters (E), Homer1 levels (F), and Homer1 disc area (G) were not consistently and significantly affected by all metalloprotease inhibitors. Data are means ± SEM. Statistical significance was determined by two-sample *t* test to treatment with vehicle (*, $P < 0.05$; **, $P < 0.01$). For B–G, *n* as number of synapses = 20, VEH; 49, GM; 45, GW; 39, GI; 20, C3/three cultures. For further details, see Fig. S5.

Our study focused on excitatory synapses marked by the presence of Homer1, with Nrxn1 visualized both via a knocked-in HA-epitope tag and by application of a pan-neurexin antibody. Our conclusion that Nrxn1 assembles into a novel, dynamically regulated nanocluster in excitatory synapses thus is based on four major lines of evidence. First, using 3D STORM imaging, we found that Nrxn1 could be detected in synaptic nanoclusters that occupy 15–20% of the synaptic cleft area, with most Nrxn1(+) synapses having only a single nanocluster (Figs. 3, 4, 5, 6, 10, S1, S2, S4, and S5). Second, we found that Nrxn1 is present at more active synapses, which contain higher levels of synaptic vesicle exocytosis and surface GluA1, than synapses without Nrxn1 nanoclusters (Fig. 6). Third, we found that Nrxn1 is physiologically processed by ectodomain proteases, with the dominant contribution of proteolytic cleavage coming from ADAM10 that cleaves Nrxn1 at a site between the Cys-loop domain and transmembrane region (Figs. 2, 7, 8, 9, 10, and S5). As a result of ectodomain cleavage, ∼6% of Nrxn1 in adult mouse cortex is present as the released extracellular fragment; in contrast, the previously characterized ectodomain cleavage of neuroligin-1 (Peixoto et al., 2012; Suzuki et al., 2012) causes a release of only ∼2% of the extracellular neuroligin-1 fragment in

adult cortex (Fig. 8 E). Fourth, pharmacological inhibition of ADAM10 proteolysis in cultured hippocampal neurons caused a substantial increase in both the number of synapses containing Nrxn1 nanoclusters and the Nrxn1 content of Nrxn1 nanoclusters (Fig. 10), while not significantly affecting excitatory synapse number (Fig. S5, J–R). Remarkably, ADAM10 inhibition did not cause a significant change in total Nrxn1 protein, although it did decrease the release of the extracellular Nrxn1 fragment by >60% (Fig. 9). These findings show that ADAM10 inhibition caused not only a decrease in Nrxn1 proteolytic turnover, but also a redistribution of Nrxn1 from a "free" state into synaptic nanoclusters. Since ADAM10 is a versatile multifunctional protease that is tightly regulated (Saftig and Lichtenthaler, 2015; Saint-Pol et al., 2017), these data suggest that Nrxn1 nanoclusters can be controlled via regulation of ADAM10. Based on these data, a plausible mechanism would be that Nrxn1 molecules are continuously recruited to the nanoclusters and released into the extracellular space via ectodomain cleavage by ADAM10, thus maintaining Nrxn1 nanoclusters in a dynamic equilibrium.

Is it possible that the nanoclusters constitute experimental artifacts? We raise this question particularly because we first identified the Nrxn1 nanoclusters using knockin mice in which endogenous Nrxn1 was tagged, which may have changed its properties. To address these concerns, we showed that Nrxn1 nanoclusters were similarly observed, with identical properties and similar developmental dynamics, in cultured hippocampal neurons and in hippocampal sections (Figs. 3, 4, and S1), and that the same nanoclusters were detected independent of labeling and fixation conditions (Fig. 5 and Fig. S2). Most importantly, we identified the same nanoclusters using a pan-neurexin antibody and neurons expressing unmodified neurexins (Fig. 5 and Fig. S2) and also identified that HA-Nrxn1 and pan-neurexin signals mostly colocalized (Fig. 5, I–N). Finally, we documented that the nanoclusters were abolished upon genetic deletion of neurexins 1, 2, and 3 (Fig. 5, E–H). We believe that these observations together rule out conceivable artifacts. A recent immunoelectron microscopy study using the same pan-neurexin antibodies that we applied for control labeling obtained results consistent with a nonrandom distribution of neurexins (Szoboszlay et al., 2017).

The discovery of Nrxn1 nanoclusters in excitatory synapses raises new questions. For example, do Nrxn2 and Nrxn3 also assemble into these nanoclusters, how do the nanoclusters form, and does alternative splicing of neurexins regulate the nanoclusters? Partial answers to the first question are already provided by our experiments demonstrating that upon deletion of only Nrxn1, the pan-neurexin antibody still detects synaptic nanoclusters, whereas deletion of all neurexins abolishes synaptic neurexin nanoclusters (Fig. 5). This result reveals that Nrxn2 and/or Nrxn3 detected by the pan-neurexin antibody must also be present in the nanoclusters. Regarding the mechanism of neurexin nanocluster formation, it seems likely that interactions of their cytoplasmic tail with the cytoskeleton (Biederer and Sudhof, 2001; Rui et al., 2017) or specific features of their glycosylation (Zhang et al., 2018) may be important, although testing this will be difficult since overexpression of mutant proteins is likely to introduce unintended side effects. Finally, the issue of alternative splicing seems particularly important given the close proximity of SS5 to the region of ADAM10 cleavage in Nrxn1 (Figs. 7, 8, 9, and S5), providing a possible mechanism for alternative splicing to regulate both neurexin cleavage and nanocluster dynamics. However, these three questions are only the proverbial tip of the iceberg with regard to synapse organization and neurexin function, an overall question that will occupy the field for years to come.

Materials and methods

Generation of HA-Nrxn1 cKI mice

In generating HA-tagged neurexin-1 cKI mice, we aimed to (1) introduce a double HA tag (2xHA-tag) to allow the detection of the HA-epitope–tagged Nrxn1 including α-, β-, and -γ isoforms, and (2) to introduce a single loxP site into the reading frame to allow for Cre-mediated in-frame recombination resulting in truncated Nrxn1 proteins (Fig. 1 A). Transgenic mice were generated by homologous recombination in R1 embryonic stem (ES) cells (Tabuchi et al., 2007) using the strategy outlined in Fig. S1 A that targets the last exon of *Nrxn1*, exon-26 (Tabuchi and Südhof, 2002; Treutlein et al., 2014). Briefly, immediately after the first two bases of *Nrxn1* exon-26, in maintaining frame order, we introduced the coding sequence of two hemagglutinin motifs (amino acid sequence: YPYDVPDYAYPYDVPDYA) as well as the 34-bp sequence of a WT loxP site complemented by two additional bases to avoid a frame shift and a *SpeI* restriction site for cloning purposes. The amino acid sequence of the translated loxP site including the two additional bases and the *SpeI* site within the mutated full exon 26 reads as follows: ITSYSIHYTKLSTS. The second loxP site was introduced immediately downstream of the endogenous stop codon. Upon Cre/loxP-mediated recombination, the coding region now terminates in a stop codon shortening the translated loxP site into the sequence ITSYSIHYTKL. Since the transmembrane region is encoded by the sequence downstream of the introduced loxP site, Cre/loxP-mediated recombination will result in a truncated Nrxn1 protein lacking its membrane anchoring sequence and intracellular C-terminus.

The 3′ loxP site is followed by a frt site–flanked neomycin resistance gene under control of the phosphoglycerate-kinase promoter, PGK-neo^R, to allow for the selection of homologously recombined ES cells. The mutated *Nrxn1* exon 26 and the selection cassette were both flanked by ∼6-kb homology regions, respectively. Additionally, upstream of the 5′ homology region, a diphtheria toxin minigene was inserted for negative selection. Electroporation into (129X1/SvJ x 129S1/Sv)F1-*Kitl*$^+$-derived R1 ES cells, drug selection, and clone isolation were performed as previously described (Nagy et al., 2006; University of Texas Southwestern Transgenic Facility, Dallas, TX). Positive ES clones were identified by Southern blotting and PCR genotyping. Blastocyst injection was performed by the Stanford Transgenic Facility, Stanford, CA. Chimeric offspring were bred to C57BL/6 mice to select for the recombined allele. Mutated mice were subsequently bred to Flp-deleter mice (Rodríguez et al., 2000) for the removal of the frt-flanked selection cassette, *Nrxn1*^{KI} allele, and Cre-deleter mice (Schwenk et al., 1995)

generating the *Nrxn1* truncated allele, *Nrxn1*^{tr}. Both deleter mouse lines were maintained on a C57BL/6 background (JAX stock #003800 [Flp-deleter] and #006054 [Cre-deleter]), and Nrxn1 cKI mice have been bred several rounds to C57BL/6 mice with the intention to remove the transgenic Flp- and Cre-alleles so that all experiments were performed on congenic backgrounds of at least 95% C57BL/6 unless noted differently. The HA-Nrxn1 cKI mouse line was deposited with the Jackson Laboratory Mouse Repository for distribution (B6.129-*Nrxn1*^{tm3Sud}/J, stock #021777).

All mouse work was performed as prescribed by approved protocols at Stanford University. Mice were weaned at 20 d of age and housed in groups of up to five on a 12-h light/dark cycle with food and water ad libitum. Animals were kept in the Stanford Animal Housing Facility with all procedures conforming to the standards set by the National Institutes of Health Guidelines for the Care and Use of Laboratory Mice and approved by the Stanford University Administrative Panel on Laboratory Animal Care.

The following primers were used for genotyping to discriminate between different alleles: MX10434, 5′-GCCTTGAGA GGGTGAACACTTTATTTGG-3′; MX10435, 5′-CCATTGGACTGT GCTGAGTTACTGATG-3′; and MX10472, 5′-TTTGCTTTATGA ATGCGTGCGGTCCTCACC-3′.

Oligonucleotide combinations MX10434/MX10435 were used to identify the presence of *Nrxn1*^{wt} (382 bp) and *Nrxn1*^{KI} (472 bp) alleles; MX10434/MX10472 identified the *Nrxn1*^{tr} (682 bp) allele.

Survival analyses were performed by comparing the genotype distribution observed in litters resulting from *Nrxn1*$^{wt/tr}$ x *Nrxn1*$^{wt/tr}$ (het x het) crosses at either P1 or P21. Observed genotype distribution was compared with expected distribution based on Mendelian inheritance (Kaeser et al., 2008). A chi-square test was used to determine whether the observed offspring ratio differed significantly from the expected ratio.

Cell culture

Primary neuronal culture

Hippocampal, olfactory bulb, and cortical neurons were cultured from newborn mice as described previously (Maximov et al., 2007) with some modifications. Dissected hippocampi, olfactory bulbs, or cortices were digested for 20 min with 10 U/ml papain in Hank's buffered saline (HBS) in an incubator, washed with HBS, dissociated in plating media (MEM supplemented with 0.5% glucose, 0.02% $NaHCO_3$, 0.1 mg/ml transferrin, 10% FBS, 2 mM L-glutamine, and 0.025 mg/ml insulin), and seeded on Matrigel (BD Biosciences) precoated coverslips placed inside 24-well dishes. The day of plating was considered as DIV0. After 24 h (DIV1), 95% of the plating medium was replaced with neuronal growth medium (Neurobasal-A medium supplemented with 2% B27 supplement and 0.5 mM L-glutamine). At DIV2–3 (for hippocampal and olfactory bulb cultures) or DIV3–4 (for cortical cultures), 50% of the medium was exchanged with fresh growth medium additionally supplemented with 4 µM AraC (Sigma-Aldrich) to restrict glial overgrowth. When applicable, lentivirus supernatants were always added on DIV3–4 following exchange of media. For long-term culture of neurons, 25% fresh media was added every 4–5 d starting from DIV7. Most imaging experiments used P0 pups from HA-Nrxn1 cKI mice. For biochemistry experiments, HA-Nrxn1 cKI cultures were prepared simultaneously from newborn HA-Nrxn1 cKI mice, and WT cultures were prepared from newborn CD1 mice. For select control experiments, cultures were also prepared from Nrxn1 cKO mice and Nrxn1/2/3 cKO mice (Chen et al., 2017). For generation of cultures from P0 pups, gender was not taken into account. In general, pooling tissue from three to six mice in a given preparation was used to generate cultures.

HEK293T cells

WT HEK293T cells were maintained in DMEM supplemented with 10% FBS, penicillin, and streptomycin. For producing lentivirus, cells were transfected using the calcium phosphate method (as described below).

Real-time quantitative RT-PCR (qRT-PCR)

Brain tissue

For qRT-PCR analysis, age-matched adult (10 wk old) males from the same litters were used and were either homozygous for the *Nrxn1* WT locus (WT mice) or carried a single truncated allele, *Nrxn1*$^{wt/tr}$ (n = 4 per genotype). Mice were euthanized using isoflurane, and the entire was brain dissected and then collected in TRIzol reagent. RNA was isolated according to the manufacturer's protocol (Invitrogen). RNA concentration was measured using an ND-1000 spectrophotometer (Thermo Fisher Scientific). Briefly, reactions were loaded onto an ABI7900 fast RT-PCR machine (Applied Biosystems) and run in triplicates with 100 ng RNA per run using VeriQuest Probe one-step qRT-PCR master mix with ROX (Affymetrix). Gene-specific qPCR assays were purchased from Integrated DNA Technologies, and mouse ACTB assay (4352933E) was purchased from Applied Biosystems. The following PrimeTime qPCR Assays (IDT) were used (shown as gene, primer1, probe, primer2): Nrxn1α, 5′-TCCTCTTAGACATGGGAT CAGG-3′, 5′-CAACGGGATGGACGGTCAGGTA-3′, 5′-GTGTAGGGA GTGCGTAGTG-3′; Nrxn1β, 5′-TGGCCCTGATCTGGATAGTC-3′, 5′-ACCACATCCACCATTTCCAT-3′, 5′-AATCTGTCCACCACCTTTGC-3′; Nrxn2α/β, 5′-ATCATCACTTGGACACTCAGC-3′, 5′-CAGGAG GTCATCTGTGTTCTGGGTG-3′, 5′-ACAATGAGGGACAGCACC-3′; Nrxn2α, 5′-GTCAGCAACAACTTCATGGG-3′, 5′-CTTCATCTTCGG GTCCCCTTCCT-3′, 5′-AGCCACATCCTCACAACG-3′; Nrxn2β, 5′-CCACCACTTCCACAGCAAG-3′, 5′-GGACCACATACATCTTCGGG-3′, 5′-CTGGTGTGTGCTGAAGCCTA-3′; Nrxn3α/β, 5′-CCTTTGTCC TTTCCTCCGATG-3′, 5′-TTTTCCTGCAGCCACTCCTCTACG-3′, 5′-CACTGATAATGAACGCCTCCA-3′; Nrxn3α, 5′-GGGAGAACCTGC GAAAGAG-3′, 5′-CTGCCGTCATAGCTCAGGATAGATGC-3′, 5′-ATGAAGCGGAAGGACACATC-3′; Nrxn3β, 5′-CACCACTCTGTG CCTATTTC-3′, 5′-TCTATCGCTCCCCTGTTTCC-3′, 5′-GGCCAG GTATAGAGGATGA-3′; Nlgn1, 5′-GGTTGGGTTTGGTATGGATGA-3′, 5′-TGAGGAACTGGTTGATTTGGGTCACC-3′, 5′-GATGTTGAG TGCAGTAGTAATGAC-3′; Nlgn2, 5′-CCGTGTAGAAACAGCATG ACC-3′, 5′-TCAATCCGCCAGACACAGATATCCG-3′, 5′-TGCCTG TACCTCAACCTCTA-3′; Nlgn3, 5′-CACTGTCTCGGATGTCTTCA-3′, 5′-CCTGTTTCTTAGCGCCGGATCCAT-3′, 5′-CCTCTATCTGAA TGTGTATGTGC-3′; LRRTM2, 5′-GGCCACTTGAAATGTAAGCC-3′, 5′-TGCAGCCTCCAATGTGCTCAGAA-3′, 5′-CACTGCGTTGAGTCT GACAA-3′; LRRTM3, 5′-CATATGCCAGAAAGGTTGACAC-3′,

5′-AGGCTCCAGGGAATGTGAGATACCT-3′, 5′-GAGATGCTGCTG AACGGAA-3′; LRRTM4, 5′-GAAATAGCACCAGAAACACACTC-3′, 5′-ACGGAAACCCATCCTTTGTCATCCA-3′, 5′-GACCAAATAAGA AGAAAGCTGAGAG-3′; Lphn1, 5′-GACTGATGCTCTGACTCATGT-3′, 5′-TGGGCACACGAAGATGTAAGGGAC-3′, 5′-CTGGAACCT ACAAATACCTGGA-3′; Lphn2, 5′-CTCGTGGTGGATATTGTGGTT-3′, 5′-TGACCCTGCCCAAGTGCCTAC-3′, 5′-TTACGGTATTCCCTG GAGTTTG-3′; and Lphn3, 5′-AGAAACATCCAGGTGAAGGC-3′, 5′-AAGAAATGCAAAAGAGCCGCGAACA-3′, 5′-GAATCAACAGAA CCGACCAAC-3′. The Nrxn1-HA assay was designed to identify the presence of the mutated alleles (*Nrxn1*^{KI} and *Nrxn1*^{tr}). For this purpose, in the assay the sense oligo (5′-ACAGATGACATCCTT GTGGC-3′) and the probe (5′-ACATTGACCCCTGTGAGCCGAG-3′) are both located in the proceeding exon, while the antisense oligo (5′-GTTATAGCATAGTCAGGTACGTCG-3′) is located in the mutated sequence of exon 26 including parts of the HA coding sequence and the first five bases of the loxP site. The relative transcript level of the target mRNA in each sample was calculated by normalization of cycle threshold (CT) values to the reference mRNA (β-actin) using the following equation: $V = 2^{CT[reference]}/2^{CT[target]}$; V is the relative value of target gene normalized to the reference.

Primary neurons

RNA was isolated from DIV12 neurons that had been previously infected with lentivirus on DIV3–4 to allow Cre-mediated gene deletion or knockdown of ADAM10 using shRNA (see below). RNA was isolated using the PrepEase RNA spin kit according to the manufacturer's instructions (Affymetrix). Nrxn1, Nrxn3, Lphn1, and Nlgn1 probes are described above. A prevalidated mouse ADAM10 assay (assay ID: Mm.PT.58.14225600) was obtained from Integrated DNA Technologies. For each reaction, 1 µl of RNA was run in triplicate using VeriQuest Probe one-step qRT-PCR master mix with ROX (Affymetrix). Reactions were loaded onto a QuantStudio3 Real-Time PCR machine (Thermo Fisher Scientific). The relative transcript level of the target mRNA in each sample was calculated as described above.

Lentivirus production and infection

Recombinant lentiviral particles were produced in HEK293T cells by cotransfecting cells with long terminal repeat (LTR) containing vector and helper plasmids (pRSV-REV, pMDLg/gRRE, and pVSVG) using calcium phosphate. Media were exchanged 1 h before transfection and included 25 µM chloroquine diphosphate. Per 75 cm^2 of cells, 0.5 ml of 250 mM $CaCl_2$ containing molar equivalents of DNA (12 µg of LTR-containing vector, 3.9 µg pRSV-REV, 8.1 µg pMDLg/gRRE, and 6.0 µg pVSVG) was added dropwise to an equal volume of 2X-HBS (0.4 M NaCl, 10 mM KCl, 1.5 mM Na_2HPO_4, 0.2% glucose, and 38.4 mM HEPES, pH 7.05) under vigorous mixing, incubated for 20 min at room temperature, and added dropwise to the cells. 16–20 h following transfection, cells were washed with plain DMEM and replaced with neuronal growth media lacking AraC. After 24 h, media containing lentiviral particles were cleared by centrifugation (1,500 ×*g*, 10 min), aliquoted, and snap-frozen. Neuronal cultures were infected with lentivirus on DIV3 or 4 by adding 25–30 µl of viral supernatant per well of a 24-well plate.

For generating cKO cultures, matched sets of lentiviruses were produced using LTR-containing vectors that included Cre or mutant ΔCre (inactive) fused to EGFP and driven by the human synapsin-1 promoter (Kaeser et al., 2011). For gene knockdown, lentiviruses were produced using lentiviral constructs containing shRNAs against mouse ADAM10 purchased from the MISSION shRNA Library (Sigma-Aldrich). Three different shRNAs were used for ADAM10 knockdown in the pLKO.1 lentivirus expression vector, including ADAM10 shRNA 1 (The RNAi Consortium [TRC] No.: TRCN0000031844; sequence: 5′-CCGGGCAGAGAGATACAT TAAAGATCTCGAGATCTTTAATGTATCTCTCTGCTTTTTG-3′), ADAM10 shRNA 2 (TRC No.: TRCN0000031847; sequence: 5′-CCGGCAGCTCTATATCCAGACAGATCTCGAGATCTGTCTGGA TATAGAGCTGTTTTTG-3′), and ADAM10 shRNA 3 (TRC No.: TRCN0000031848; sequence: 5′-CCGGCCAGGAGAGTCTAA GAACTTACTCGAGTAAGTTCTTAGACTCTCCTGGTTTTTG-3′). All other viruses were generated using a similar lentiviral backbone as Cre, which contains the human synapsin-1 promoter to drive gene expression in neurons (described further below). For ADAM10 WT and mutant overexpression, viruses were prepared either containing no insert (control), WT ADAM10 (A10-wt), ADAM10-E384A (A10-E384A), or ADAM10 lacking its prodomain and metalloprotease domain (A10-ΔPro/MP).

Electrophysiology

For electrophysiology recordings, hippocampal neurons were prepared from newborn Nrxn1 cKO or HA-Nrxn1 cKI mice. Cultures were infected with lentiviruses carrying Cre or mutant ΔCre (inactive) fused to EGFP on DIV3. Culture coverslips were superfused with artificial cerebrospinal fluid (ACSF) solution (in mM): 120 NaCl, 2.5 KCl, 1 NaH_2PO_4, 26.2 $NaHCO_3$, 2.5 $CaCl_2$, 1.3 $MgSO_4 \cdot 7H_2O$, and 11 D-glucose, ∼290 mOsm. Miniature excitatory postsynaptic currents (mEPSCs) were recorded with an internal solution containing (in mM): 117 Cs-methanesulfonate, 15 CsCl, 8 NaCl, 10 TEA-Cl, 0.2 EGTA, 4 Na_2-ATP, 0.3 Na_2-GTP, and 10 HEPES, pH 7.3, with CsOH (∼300 mOsm). mEPSCs were recorded in ACSF containing 0.5 µM tetrodotoxin (TTX) and 100 µM picrotoxin. Miniature events were handpicked and analyzed in Clampfit 10 (Molecular Devices) using template matching. Synaptic currents were monitored with a Multiclamp 700B amplifier (Molecular Devices). Data were collected at 10 kHz and filtered with a low-pass filter at 2 kHz. For all experiments, the experimenter was blind to the recording condition.

Immunocytochemistry

For live surface-labeling experiments, primary neurons were first washed at room temperature once with a HEPES bath solution, which contained the following (in mM): 140–150 NaCl, 4–5 KCl, 2 $CaCl_2$, 1 $MgCl_2$, 10 glucose, and 10 HEPES, with pH adjusted to 7.4 with NaOH, and osmolarity of 300 mOsm. For conventional fluorescence imaging, cultures were then incubated at room temperature for 20 min with purified mouse anti-HA monoclonal antibody (1:250; anti-HA.11; BioLegend) diluted in HEPES bath solution. For STORM imaging experiments, cultures were incubated with the same antibody dye labeled with 405–647 (1:250) in HEPES bath solution at room temperature for 20 min. For double-labeling Nrxn1

nanoclusters with markers for synapse activity, dye-labeled anti-HA 405–647 was co-incubated with either anti-GluA1 (PC246; Calbiochem) at 1:10 or an antibody recognizing the luminal domain of synaptotagmin-1 (105103; Synaptic Systems) at 1:100 for 20 min at room temperature. Cultures were then gently washed three times with HEPES bath solution, followed by fixation for 20 min at room temperature with 4% (wt/vol) PFA. Following fixation, cultures were washed three times with Dulbecco's PBS (DPBS). For surface-labeling experiments to be used for conventional imaging, cultures were blocked for 1 h at room temperature with antibody dilution buffer (ADB) without Triton X-100(−), which contains 5% normal goat serum diluted in DPBS. Cells were then labeled with Alexa Fluor–conjugated secondary antibodies (1:1,000; Invitrogen) diluted in ADB(−) for 2 h at room temperature. Cells were washed and then permeabilized and blocked for 1 h with ADB with Triton X-100(+), which contains 0.2% Triton X-100 and 5% normal goat serum diluted in DPBS. Nonsurface primary antibodies were diluted in ADB(+), and cells were incubated overnight at 4°C. Cultures were washed three times and then incubated with either Alexa Fluor–conjugated secondary antibodies (1:1,000; Invitrogen) or STORM secondary antibodies (1:250; described below) in ABD(+) for 2 h. Following three washes, coverslips for conventional imaging were inverted onto glass microscope slides with Fluoromount-G mounting media (Southern Biotech). For STORM imaging, samples were stored in the dark at 4°C until further processing, for no longer than 1 wk until downstream processing.

For non–surface-labeled stains, cultures were first washed once with DPBS followed by a 20-min fixation at room temperature with 4% (wt/vol) PFA. Following fixation, cultures were washed three times with DPBS. For stronger fixation (as used for Fig. S2, F–J), cultures were incubated with 3% PFA and 0.1% glutaraldehyde for 20 min, followed by treatment with sodium borohydride (1 mg/ml, 12-min incubation) to quench autofluorescence. Cultures were incubated for 1 h with ADB(+), followed by overnight incubation at 4°C with antibodies diluted in ADB(+). Coverslips were washed three times and then incubated for 2 h with either Alexa Fluor–conjugated secondary antibodies (1:1,000; Invitrogen) or STORM secondary antibodies (1:250) in ABD(+). Coverslips were further processed as described above for surface-labeled specimens.

The antibodies used for conventional imaging included the following: rabbit anti-HA (1:250; #3724; Cell Signaling), mouse anti-HA monoclonal antibody (1:1,000 for prefixed; anti-HA.11; BioLegend), rabbit anti-Homer1 (1:500; 160003; Synaptic Systems), guinea pig anti-Homer1 (160004), rabbit anti-vGluT1 (1:1,000; YZ6089; TCS), rabbit anti-synapsin (1:500; E028; TCS), guinea pig anti-vGluT1 (1:500; AB5905; Millipore), rabbit anti-VGAT (1:500; AB5062P; Millipore), chicken anti-MAP2 (1:1,000; CPCA-MAP2; Encor), rabbit anti–Munc13-1 (1:500; 126103; Synaptic Systems), and rabbit anti-RIM1/2 (1:500; 140203; Synaptic Systems). The antibodies used for STORM imaging included the following: rabbit anti–pan-neurexin (1:250; Af870; Frontier Institute), rabbit anti-Piccolo (1:200; 142003; Synaptic Systems), rabbit anti-Bassoon (1:200; 141003; Synaptic Systems), mouse anti-Homer1 (1:500; 160011; Synaptic Systems), and rabbit anti-Homer1 (1:500; 160003; Synaptic Systems). For STORM imaging, neurexin-1–HA or pan-neurexins were directly labeled with mouse HA and rabbit anti–pan-neurexin (1:250; Af870; Frontier Institute) that had been preconjugated with 405–647 dye pairs (see below). Remaining antibodies used for STORM were recognized by dye-labeled secondary antibodies (described below).

For conventional microscopy (Figs. 2, S1, S3, and S5), confocal images were acquired at room temperature using an inverted Nikon A1 Eclipse Ti confocal microscope (Nikon) equipped with a 60× objective (Apo, NA 1.4) and operated by NIS-Elements AR acquisition software. Images were taken at 1,024 × 1,024 pixels with a z-stack distance of 0.5 µm. Images were acquired sequentially in order to avoid bleed-through between channels. Imaging parameters (i.e., laser power, photomultiplier gain, scan speed, etc.) were optimized to prevent pixel saturation and kept constant for all conditions within the same experiment. Images were analyzed using NIS-Elements Advanced Research software (Nikon).

Excitatory synapse quantification

For Fig. S3, three or four independent cultures were prepared, and separate wells were infected with lentivirus carrying Cre or ΔCre. At DIV14, cultures were fixed and stained as described above for either vGluT1, total HA, Homer1, and MAP2 (for Nrxn1 cKI) or just MAP2 and vGluT1 (for Nrxn1 cKO). For Fig. S5, J–R, DIV10 HA-Nrxn1 cKI hippocampal neurons were incubated for 48 h with GI250423X followed by fixation and staining of vGluT1, MAP2, and Homer1 on DIV12. For all experiments, 9–10 neurons were blindly selected for both Cre and ΔCre groups per culture. Neurons were always confirmed to be healthy (i.e., continuous processes) and have pyramidal morphology by viewing the MAP2 staining. General Analysis was performed with NIS-Elements, and binaries were generated following background subtraction applied equally to groups being compared and imaged on the same day. Binary operations were used to distinguish Homer1 and vGluT1 puncta associated with MAP2. Two regions of interest were blindly drawn on secondary and tertiary dendrites of imaged pyramidal neurons. Quantification of puncta density, area, and intensity was averaged per culture before statistical analysis.

Sample preparation, imaging, and analysis for STORM

Tissue preparation

Hippocampal tissue slices were prepared for STORM imaging following a modified protocol described previously (Dani et al., 2010). Specifically, mouse brains that have been perfusion fixed with 4% PFA (Electron Microscopy Sciences) were cryoprotected by immersion in 30% sucrose (Sigma-Aldrich) overnight and embedded in a 2:1 mixture of 30% sucrose:TissueTek OCT Compound (Sakura). Frozen tissue blocks were cut into 10-µm sections on a cryostat and collected on glass slides (Thermo Fisher Scientific). Sections were blocked with 5% BSA (Jackson ImmunoResearch) in 1× DPBS and incubated with anti-HA tag (HA; BioLegend) antibody labeled with Alexa Fluor 405 and Alexa Fluor 647 (Thermo Fisher Scientific) dyes following previously described protocols (Bates et al., 2007) for

30 min at room temperature in 5% BSA in 1× DPBS and washed three times for 15 min each with 1% BSA in DPBS. Sections were then permeabilized with 0.1% wt/vol saponin (Sigma-Aldrich) in 5% BSA in 1× DPBS for 30 min and stained overnight at 4°C in 5% BSA in 1× DPBS with antibodies against Homer1 (1:400; Synaptic Systems), Piccolo (1:400; Synaptic Systems), or Bassoon (1:400; Enzo Life Sciences). After washing three times with 1% BSA in PBS, samples were stained for 2 h at room temperature with appropriate secondary antibodies (Jackson ImmunoResearch) labeled with Alexa Fluor 647 and Cy3 (Invitrogen) in 5% BSA in 1× DPBS, and washed three times with 1% BSA in 1× DPBS. Sections were then immediately imaged.

Imaging buffer and sample mounting

The STORM imaging buffer was prepared with 100 mM cysteamine (Sigma-Aldrich), 5% wt/vol D-glucose (Sigma-Aldrich), 0.8 mg/ml glucose oxidase (Sigma-Aldrich), and 40 µg/ml catalase (Sigma-Aldrich) in 1× DPBS. For tissue sections, 100 µl imaging buffer was dropped onto glass slides holding the cryosection, and covered with a #1.5 rectangular glass coverslip (22 mm × 30 mm; Thermo Fisher Scientific). Excess imaging buffer was wicked away, and the sample was sealed using nail polish. For cultured neuron sections, 150 µl imaging buffer was first deposited into an imaging chamber before the sample coverslip was inverted over the chamber and pressed down firmly before sealing with nail polish.

STORM setup

STORM imaging experiments were conducted on a custom-built Nikon Eclipse-Ti inverted microscope with illumination channels at 405 nm (OBIS 405-LX; Coherent), 460 nm (Sapphire 460–10; Coherent), 488 nm (Genesis MX488-1000 STM; Coherent), 561 nm (Sapphire 561–200 CW CDRH; Coherent), and 647 nm (F-04306–113; MPB Communications). Lasers were introduced through the backport of the microscope, passing through a ZT405/488/561/647/752RPC (Chroma) dichroic mirror and a ZET405/488/561/647–656/752 penta-band notch (Chroma) emission filter. A translation stage allowed the incident beams to be directed at low incidence angles to illuminate only fluorophores near the coverglass (i.e., within ∼1–2 µm of the coverglass). For 3D imaging, a Roper Scientific Dual View system was inserted between the microscope body and the EMCCD camera (iXon; DU-897E-CSO-#BV; Andor), where a 1-m focal length cylindrical lens was inserted in place of a beamsplitter. Focus was maintained via a custom-built feedback system in which an 850-nm infrared laser was directed into the objective back aperture, and its reflection from the glass/liquid interface was imaged onto a quadrant photodiode, driving a piezo objective nanopositioner (Nano F-100; Madcity Labs).

STORM imaging and analysis

For two-color STORM imaging, the 405- and 561-nm lasers were used to activate the corresponding Alexa Fluor 405–Alexa Fluor 647 or Cy3–Alexa Fluor 647 dye pair, and the 647-nm laser was used to both excite Alexa Fluor 647 fluorophores and switch them into the dark state. STORM movies were acquired at 60 Hz until most dyes were photobleached within the field of view. During acquisition, the power of the activation lasers (405 nm and 561 nm) was gradually adjusted so that only a small subset of fluorophores was activated in any frame, allowing individual activated molecules to be imaged and localized, and the two-color channels were roughly even in their activation. The 647-nm laser was maintained at ∼80 mW throughout the experiment, while the 405-nm and 561-nm lasers were ramped up to a maximum of 2 mW and 1 mW, respectively. The illumination lasers were either mechanically or digitally shuttered in four-frame events consisting of one frame of activation laser (405 or 561 nm) and three frames of imaging laser (647 nm), and alternating in the activation channels (i.e., between 405 nm and 561 nm) for four frames in each channel. STORM movies were automatically analyzed using custom-written software implementing 3D-DAOSTORM (Babcock et al., 2012), generating molecule lists for each STORM image that could be used for subsequent analyses. In brief, the x and y positions of the fluorophores are determined from the centroid positions of their images, and the z position of the fluorophores is determined from the ellipticity of their images, as previously described (Rust et al., 2006; Huang et al., 2008). Cross-talk between color channels was subtracted using methods previously described for activator-based multi-color STORM (Dani et al., 2010). For three-color imaging, a conventional image was acquired using the 488-nm laser to excite Alexa Fluor 488, labeling Homer1, in addition to the two-color STORM image.

Synapse selection

To select synapses in two-color STORM images, homer localizations were first clustered through an implementation of DBSCAN with a distance of 80 nm and a minimum of 5 points per assigned cluster. To be designated as a synapse, a homer cluster must contain at least 100 localizations, and the spatial distribution of localizations in the cluster must have two dimensions as least twice as large as the third dimension. Synapses were then defined as the homer cluster, as well as all neurexin localizations within 500 nm of the edge of the homer cluster.

STORM localizations from synapses were plotted based on their coordinates to create STORM images of individual synapses, which were rotated such that the trans-synaptic axis aligned along the x axis, with the synaptic protein signal, e.g., homer, toward the negative side. By defining the origin as the centroid of the homer signal, both trans-synaptic and radial distances (defined as $R = \sqrt{y^2 + z^2}$) could be calculated. To determine the normalized radial distance R_{Norm}, a radius was determined for each synapse, R_{95}, which defined a ring encompassing 95% of homer localizations. R_{Norm} could then be calculated as a simple ratio of the two values: $R_{Norm} = R/R_{95}$. Neurexin and homer levels were calculated from cross-talk–subtracted localization counts for each synapse. The number of neurexin clusters per synapse was determined by applying an implementation of DBSCAN to identify and count the number of neurexin clusters in each synapses. HA antibodies per cluster were estimated by first determining the average number of localizations per isolated antibody, L_{AB}, and then dividing the number of localizations per neurexin cluster, L_{Nxn}, by the value of L_{AB}. Neurexin and homer areas were

calculated via a coarse convex hull method, where 2D bins of 35 × 35 nm were first defined on the geometric plane parallel to the synaptic face, and centered around the centroid of the homer cluster. The cluster area was then defined as the sum of the area of bins containing at least two STORM localizations (to eliminate spurious outliers) after cross-talk subtraction. Two alternative methods of area measurements (i.e., convex hull area and radius of gyration based on the localizations) were also compared, and produced results with similar trends to those obtained from the coarse convex hull quantification. Although the same trends were observed from all three methods, quantitative numbers differed (Fig. S1 P), likely because these methods have different sensitivities to outliers and holes (convex hull is more sensitive to outliers than coarse convex hull and radius gyration, and convex hull and radius gyration do not detect holes unlike coarse convex hull).

For three-color imaging experiments, synapses were defined by the area of homer puncta in the conventional image. The degree of cluster volume overlap was calculated for the two neurexin antibody labels using two methods. The first method is based on the coarse convex hull method described above but extended to 3D to determine cluster volume. The overlap fraction is calculated as the number voxels containing STORM localizations in both antibody channels divided by the total number of voxels that contain STORM localizations regardless of antibody channels. The second method is the convex hull method. The overlap fraction is calculated as the volume of overlapping region covered by the convex hulls of both antibody channels divided by the volume of the entire region covered by two convex hulls.

The STORM resolution was determined by measuring x/y/z localization SD for 100 isolated antibodies adhered to the surface of a coverslip and multiplying the average SD by 2.35 to obtain full width at half maximum (FWHM). We obtained FWHM values of 30 nm and 28 nm for x and y dimensions, respectively, and 67 nm for z (axial resolution).

Generation of expression vectors

Lentiviral vectors for expression of Cre and ΔCre (truncated, inactive) recombinase driven by the human synapsin-1 promoter have been described previously (Kaeser et al., 2011). For all other experiments using the lentiviral backbone with a human synapsin-1 vector, an empty vector was used as a control. ADAM10 shRNA expression constructs were in the pLKO.1 lentivirus expression vector (Sigma-Aldrich), including ADAM10 shRNA 1 (TRC No.: TRCN0000031844), ADAM10 shRNA 2 (TRC No.: TRCN0000031847), and ADAM10 shRNA 3 (TRC No.: TRCN0000031848). To generate ADAM10 expression constructs, the mouse ADAM10 ORF was purchased from GE Dharmacon (OMM5895-202525673). In-Fusion cloning (Clontech) was used to clone WT ADAM10 and mutants (according to the manufacturer's instructions). A catalytically inactive version of ADAM10 was generated by mutating Glu→Ala at position 384 (Lammich et al., 1999). Another dominant-negative version of ADAM10 was generated by deleting the prodomain and metalloprotease domain as previously reported (Seegar et al., 2017). A Flag epitope tag (DYKDDDDK) was included at the 3′ end of all ADAM10 constructs. Due to toxicity of the ADAM10 constructs when expressed in normal copy number *Escherichia coli*, we used Copy Cutter (Lucigen) low-copy number, inducible *E. coli* for successful cloning and generation of ADAM10 plasmids.

Immunoprecipitation

To remove debris, media from neurons were centrifuged at 3,000 rpm for 5 min. Media was carefully transferred to a new tube and a final concentration of 0.5× cOmplete ULTRA protease inhibitor cocktail (Sigma-Aldrich), and 2 mM EDTA was added. Then 30 µl of prewashed 1:1 HA agarose beads (Sigma-Aldrich) was added, and samples were rotated overnight at 4°C. Beads were washed one or two times with ice-cold DPBS before elution with 2× Laemmli buffer containing fresh DTT (100 mM) at 60°C for 10 min.

Cell lysis

Primary neurons plated in 24-well plates were isolated with 50–80 µl of complete radioimmunoprecipitation assay (RIPA) lysis buffer (cRIPA) per well with 350 µl modified cRIPA containing 150 mM NaCl, 5 mM EDTA, 1% Triton X-100, 0.1% SDS, and 25 mM Tris-HCl, pH 7.6. cRIPA also contained freshly added 1× cOmplete ULTRA protease inhibitor cocktail (Sigma-Aldrich). Lysates were incubated on ice for 20 min and then clarified by centrifugation for 20 min at 13,000 rpm at 4°C. The same volume of lysis buffer was always used for wells being compared within a given experiment. Lysates were stored at −80°C until further processing.

Immunoblotting

Proteins were separated by SDS-PAGE using 4–20% MIDI Criterion TGX precast gels (Bio-Rad). Proteins were transferred onto nitrocellulose membranes for 10 min at 2.5 V using the Trans-blot turbo transfer system (Bio-Rad). Membranes were blocked in 5% milk diluted in PBS or TBS for 1 h at room temperature. Membranes were then incubated with primary antibodies diluted in TBST (containing 0.1% Tween-20) overnight at 4°C. The following antibodies were used: HA monoclonal antibody (1:1,000; anti-HA.11; BioLegend), CASK (1:1,000; 75–000; Neuromab), PSD-95 (1:500; 73–028; Neuromab), synapsin (1:500; E028; TCS), CamKII (1:1,000 MAB8699; Millipore), synaptophysin (1:1,000; MAB5258; Millipore), Mint1 (1:500; P730; TCS), SNAP-25 (1:500; P913; TCS), Nlgn1 (1:1,000; 4C12; Synaptic Systems), GluA1 (1:1,000; Ab1504; Millipore), syntaxin-1 (1:500; 438B; TCS), Tau (1:1,000; MAB361; Millipore), ApoE (1:1,000; 701241; Thermo Fisher Scientific), HSC70 (1:1,000; 903A; TCS), Grp78 (1:1,000; Abcam), α-synuclein (1:1,000; Q698; TCS), pan-neurexin (1:500; Sudhof; A473), SynCAM4 (1:500; 75–247; Neuromab), GDI (1:2,000; 130001; Synaptic Systems), CASPR2 (1:500; 73–075; Neuromab), actin (1:2,000, A1978; Sigma-Aldrich), and Munc18 (1:1,000; 610337; BD Biosciences). Actin was used as a loading control for protein quantifications.

Combinations of the following IRDye secondary antibodies were used (1:10,000 in TBST with 5% milk): IRDye 800CW donkey anti-mouse (926–32212), IRDye 680LT donkey anti-mouse (926–68022), IRDye 800CW donkey anti-rabbit (926–32213), and IRDye 680LT donkey anti-rabbit (926–68023), from LI-COR. Detection of the

signal was obtained by Odyssey CLx imaging systems (LI-COR). Pseudo colors were applied to the signals, and quantification was performed using Image Studio 5.2 free software.

Studying processing in neurons

At DIV10, the media of hippocampal neurons or cortical neurons from HA-Nrxn1 cKI cultures were swapped with media from age-matched WT cultures supplemented with DMSO (0.1%), GM6001 (10 µM), TAPI-2 (10 µM), GW280264X (10 µM), GI254023X (20 µM), SB-3CT (30 µM), or C3 (1 µM). At 48 h after swap, media were clarified by centrifugation at 3,500 rpm for 5 min, supplemented with protease inhibitors, and incubated overnight with 30 µl of 1:1 HA-agarose beads. Cells were lysed using RIPA-containing protease inhibitor cocktail. Following two washes with cold DPBS, immunoprecipitates were eluted with 50 µl of 2× Laemmli buffer containing DTT.

For ADAM knockdown and overexpression experiments, the media of HA-Nrxn1 cKI hippocampal neurons (DIV10) were replaced with media from age-matched WT cultures. Media and cells were harvested on DIV12 and processed similar to other experiments.

For analysis of activity-dependent changes in processing, WT and HA-Nrxn1 cKI hippocampal neurons were prepared. On DIV10, media was swapped from WT neurons onto Nrxn1 cKI neurons and included 0.1% DMSO, picrotoxin (50 µM), or TTX (1 µM). Media and cell lysate were harvested 48 h later.

Fractionation

To maximize protein isolation, the average mass of dissected brain tissue (i.e., hippocampus, cortex, cerebellum, olfactory bulb, and brainstem) was predetermined for three male HA-Nrxn1 cKI mice (P56). Based on these masses, the volume used for tissue homogenization was at 40 mg/ml of buffer. For fractionation, six male HA-Nrxn1 cKI mice were euthanized using isoflurane, and fresh brain tissue was dissected on ice including the hippocampus, cortex, cerebellum, olfactory bulb, and brainstem. Until homogenization, tissue was stored in cold homogenization buffer containing 1× cOmplete ULTRA protease inhibitor cocktail (Sigma-Aldrich) and 2 mM EDTA. Tissue from one hemisphere was dounce homogenized in RIPA containing protease inhibitor cocktail (cRIPA). This tissue was incubated on ice for ≥20 min and then clarified at 14,000 rpm for 20 min at 4°C. The supernatant was saved as the total particular fraction (H).

Tissue from the other hemisphere was dounce homogenized in the same volume of ice-cold ACSF (containing in mM: 126 NaCl, 2.5 KCl, 1 NaH_2PO_4, 26.2 $NaHCO_3$, 2.5 $CaCl_2$, 1.3 $MgSO_4 \cdot 7H_2O$, 11 D-glucose, and ∼290 mOsm) with protease inhibitors (including 2 mM EDTA) for 10 strokes. Lysates were initially cleared at 13,000 rpm for 20 min (spin 1). The crude supernatant was saved, and the pellet was resuspended in equal volume as starting material of cRIPA and incubated on ice for ≥20 min. Lysates were clarified at 13,000 rpm for 20 min (spin 2), and the supernatant was saved as total particular fraction (P). The supernatant from spin 1 was further subjected to clarification for 2 h at 165,000 ×*g* (spin 3). The supernatant from spin 3 was saved as total soluble fraction (S).

For comparing the amount of Nrxn1α and Nlgn1 in particulate and soluble fractions, a bicinchoninic acid assay was performed (Thermo Fisher Scientific) according to the manufacturer's instructions. The particulate fractions were adjusted to 2 µg/µl, and soluble fractions from paired samples were adjusted with similar volumes. Proteins detected in the S fraction were much less abundant than H/P fractions, and were therefore loaded at 10 (Fig. 8 C) or 20 times (Fig. 8, D and E) more than their corresponding H or P fractions. Therefore, final measurements for Nrxn1α and Nlgn1 in the soluble fraction were divided by 20 to estimate the percentage of soluble protein relative to particular protein.

Quantification and statistical analysis

Quantification has been described in the respective Materials and methods details sections, and statistical details are provided in the figure legends. Statistical significance between various conditions was assessed by determining *P* values (95% confidence interval). For animal survival analysis and quantitative immunoblotting experiments, statistical analysis was performed using GraphPad Prism 6 software. Blot intensity quantification was performed using Image Studio Lite. Graphs depict means ± SEM. Statistical analyses for STORM images, including rank-sum tests for radial displacement and two-sample *t* tests for other quantifications, were performed in MATLAB. Values were plotted as means ± SEM.

Online supplemental material

Fig. S1 shows the targeting strategy, qRT-PCR validation results, and control data for the HA-Nrxn1 cKI mouse, showing that the truncated mRNA does not undergo nonsense-mediated decay and that HA-tagged Nrxn1 traffics to synapses. Fig. S2 shows that the Nrxn1 nanoclusters are not artifacts due to the fixation method used or the knocked-in HA-epitope. Fig. S3 shows that either truncation or loss of Nrxn1 does not alter excitatory synapse number or basic properties of synaptic transmission. Fig. S4 shows that synaptic activity does not affect the content of Nrxn1 nanoclusters or ectodomain processing, but does shift the position of nanoclusters within the synaptic cleft. Fig. S5 shows that ADAM10 shRNA and overexpression of a dominant-negative ADAM10 mutant reduce Nrxn1 ectodomain cleavage. Moreover, Fig. S5 shows that ADAM10 is not a significant regulator of excitatory synapse number in developing hippocampal cultures.

Acknowledgments

This work was supported by a National Institute of Mental Health postdoctoral fellowship (F32-MH105040 to J.H. Trotter), a Brain and Behavior Research Foundation Young Investigator Grant (20792 to T. Tsetsenis), and grants from the National Institute of Mental Health (MH052804 to T.C. Südhof), National Institute on Aging (P50AG047366 to T.C. Südhof), and National Institute of General Medicine Sciences (R35GM122487 to X. Zhuang). X. Zhuang and T.C. Südhof are investigators of the Howard Hughes Medical Institute.

The authors declare no competing financial interests.

Author contributions: J.H. Trotter, J. Hao, X. Zhuang, and T.C. Südhof designed the experiments, J.H. Trotter, J. Hao, S. Maxeiner, Z. Liu, and T. Tsetsenis performed the experiments. All authors analyzed the data. J.H. Trotter, J. Hao, X. Zhuang, and T.C. Südhof wrote the paper.

Submitted: 13 December 2018
Revised: 10 May 2019
Accepted: 30 May 2019

References

Abbott, L.F., and W.G. Regehr. 2004. Synaptic computation. *Nature.* 431: 796–803. https://doi.org/10.1038/nature03010

Anderson, G.R., J. Aoto, K. Tabuchi, C. Földy, J. Covy, A.X. Yee, D. Wu, S.J. Lee, L. Chen, R.C. Malenka, and T.C. Südhof. 2015. β-Neurexins Control Neural Circuits by Regulating Synaptic Endocannabinoid Signaling. *Cell.* 162:593–606. https://doi.org/10.1016/j.cell.2015.06.056

Aoto, J., D.C. Martinelli, R.C. Malenka, K. Tabuchi, and T.C. Südhof. 2013. Presynaptic neurexin-3 alternative splicing trans-synaptically controls postsynaptic AMPA receptor trafficking. *Cell.* 154:75–88. https://doi.org/10.1016/j.cell.2013.05.060

Babcock, H., Y.M. Sigal, and X. Zhuang. 2012. A high-density 3D localization algorithm for stochastic optical reconstruction microscopy. *Opt. Nanoscopy.* 1:6. https://doi.org/10.1186/2192-2853-1-6

Bates, M., B. Huang, G.T. Dempsey, and X. Zhuang. 2007. Multicolor super-resolution imaging with photo-switchable fluorescent probes. *Science.* 317:1749–1753. https://doi.org/10.1126/science.1146598

Biederer, T., and T.C. Sudhof. 2001. CASK and protein 4.1 support F-actin nucleation on neurexins. *J. Biol. Chem.* 276:47869–47876. https://doi.org/10.1074/jbc.M105287200

Biederer, T., P.S. Kaeser, and T.A. Blanpied. 2017. Transcellular Nanoalignment of Synaptic Function. *Neuron.* 96:680–696. https://doi.org/10.1016/j.neuron.2017.10.006

Bromer, C., T.M. Bartol, J.B. Bowden, D.D. Hubbard, D.C. Hanka, P.V. Gonzalez, M. Kuwajima, J.M. Mendenhall, P.H. Parker, W.C. Abraham, et al. 2018. Long-term potentiation expands information content of hippocampal dentate gyrus synapses. *Proc. Natl. Acad. Sci. USA.* 115: E2410–E2418. https://doi.org/10.1073/pnas.1716189115

Chen, H., A.H. Tang, and T.A. Blanpied. 2018. Subsynaptic spatial organization as a regulator of synaptic strength and plasticity. *Curr. Opin. Neurobiol.* 51:147–153. https://doi.org/10.1016/j.conb.2018.05.004

Chen, L.Y., M. Jiang, B. Zhang, O. Gokce, and T.C. Südhof. 2017. Conditional Deletion of All Neurexins Defines Diversity of Essential Synaptic Organizer Functions for Neurexins. *Neuron.* 94:611–625.e4. https://doi.org/10.1016/j.neuron.2017.04.011

Choquet, D., and A. Triller. 2013. The dynamic synapse. *Neuron.* 80:691–703. https://doi.org/10.1016/j.neuron.2013.10.013

Dai, J., J. Aoto, and T.C. Südhof. 2019. Alternative Splicing of Presynaptic Neurexins Differentially Controls Postsynaptic NMDA and AMPA Receptor Responses. *Neuron.* 102:993–1008.e5. https://doi.org/10.1016/j.neuron.2019.03.032

Dani, A., B. Huang, J. Bergan, C. Dulac, and X. Zhuang. 2010. Superresolution imaging of chemical synapses in the brain. *Neuron.* 68:843–856. https://doi.org/10.1016/j.neuron.2010.11.021

Etherton, M.R., C.A. Blaiss, C.M. Powell, and T.C. Südhof. 2009. Mouse neurexin-1α deletion causes correlated electrophysiological and behavioral changes consistent with cognitive impairments. *Proc. Natl. Acad. Sci. USA.* 106:17998–18003. https://doi.org/10.1073/pnas.0910297106

Field, J., J. Nikawa, D. Broek, B. MacDonald, L. Rodgers, I.A. Wilson, R.A. Lerner, and M. Wigler. 1988. Purification of a RAS-responsive adenylyl cyclase complex from Saccharomyces cerevisiae by use of an epitope addition method. *Mol. Cell. Biol.* 8:2159–2165. https://doi.org/10.1128/MCB.8.5.2159

Gauthier, J., T.J. Siddiqui, P. Huashan, D. Yokomaku, F.F. Hamdan, N. Champagne, M. Lapointe, D. Spiegelman, A. Noreau, R.G. Lafrenière, et al. 2011. Truncating mutations in NRXN2 and NRXN1 in autism spectrum disorders and schizophrenia. *Hum. Genet.* 130:563–573. https://doi.org/10.1007/s00439-011-0975-z

Hruska, M., N. Henderson, S.J. Le Marchand, H. Jafri, and M.B. Dalva. 2018. Synaptic nanomodules underlie the organization and plasticity of spine synapses. *Nat. Neurosci.* 21:671–682. https://doi.org/10.1038/s41593-018-0138-9

Huang, B., W. Wang, M. Bates, and X. Zhuang. 2008. Three-dimensional super-resolution imaging by stochastic optical reconstruction microscopy. *Science.* 319:810–813. https://doi.org/10.1126/science.1153529

Kaeser, P.S., H.-B. Kwon, C.Q. Chiu, L. Deng, P.E. Castillo, and T.C. Südhof. 2008. RIM1alpha and RIM1beta are synthesized from distinct promoters of the RIM1 gene to mediate differential but overlapping synaptic functions. *J. Neurosci.* 28:13435–13447. https://doi.org/10.1523/JNEUROSCI.3235-08.2008

Kaeser, P.S., L. Deng, Y. Wang, I. Dulubova, X. Liu, J. Rizo, and T.C. Südhof. 2011. RIM proteins tether Ca2+ channels to presynaptic active zones via a direct PDZ-domain interaction. *Cell.* 144:282–295. https://doi.org/10.1016/j.cell.2010.12.029

Koester, H.J., and D. Johnston. 2005. Target cell-dependent normalization of transmitter release at neocortical synapses. *Science.* 308:863–866. https://doi.org/10.1126/science.1100815

Kraszewski, K., O. Mundigl, L. Daniell, C. Verderio, M. Matteoli, and P. De Camilli. 1995. Synaptic vesicle dynamics in living cultured hippocampal neurons visualized with CY3-conjugated antibodies directed against the lumenal domain of synaptotagmin. *J. Neurosci.* 15:4328–4342. https://doi.org/10.1523/JNEUROSCI.15-06-04328.1995

Kuhn, P.-H., K. Koroniak, S. Hogl, A. Colombo, U. Zeitschel, M. Willem, C. Volbracht, U. Schepers, A. Imhof, A. Hoffmeister, et al. 2012. Secretome protein enrichment identifies physiological BACE1 protease substrates in neurons. *EMBO J.* 31:3157–3168. https://doi.org/10.1038/emboj.2012.173

Kuhn, P.-H., A.V. Colombo, B. Schusser, D. Dreymueller, S. Wetzel, U. Schepers, J. Herber, A. Ludwig, E. Kremmer, D. Montag, et al. 2016. Systematic substrate identification indicates a central role for the metalloprotease ADAM10 in axon targeting and synapse function. *eLife.* 5:e12748. https://doi.org/10.7554/eLife.12748

Lammich, S., E. Kojro, R. Postina, S. Gilbert, R. Pfeiffer, M. Jasionowski, C. Haass, and F. Fahrenholz. 1999. Constitutive and regulated α-secretase cleavage of Alzheimer's amyloid precursor protein by a disintegrin metalloprotease. *Proc. Natl. Acad. Sci. USA.* 96:3922–3927. https://doi.org/10.1073/pnas.96.7.3922

MacGillavry, H.D., Y. Song, S. Raghavachari, and T.A. Blanpied. 2013. Nanoscale scaffolding domains within the postsynaptic density concentrate synaptic AMPA receptors. *Neuron.* 78:615–622. https://doi.org/10.1016/j.neuron.2013.03.009

Maglione, M., and S.J. Sigrist. 2013. Seeing the forest tree by tree: super-resolution light microscopy meets the neurosciences. *Nat. Neurosci.* 16:790–797. https://doi.org/10.1038/nn.3403

Maschi, D., and V.A. Klyachko. 2017. Spatiotemporal Regulation of Synaptic Vesicle Fusion Sites in Central Synapses. *Neuron.* 94:65–73.e3. https://doi.org/10.1016/j.neuron.2017.03.006

Maximov, A., Z.P. Pang, D.G.R. Tervo, and T.C. Südhof. 2007. Monitoring synaptic transmission in primary neuronal cultures using local extracellular stimulation. *J. Neurosci. Methods.* 161:75–87. https://doi.org/10.1016/j.jneumeth.2006.10.009

Missler, M., W. Zhang, A. Rohlmann, G. Kattenstroth, R.E. Hammer, K. Gottmann, and T.C. Südhof. 2003. Alpha-neurexins couple Ca2+ channels to synaptic vesicle exocytosis. *Nature.* 423:939–948. https://doi.org/10.1038/nature01755

Murase, S., C.L. Lantz, and E.M. Quinlan. 2017. Light reintroduction after dark exposure reactivates plasticity in adults via perisynaptic activation of MMP-9. *eLife.* 6:e27345. https://doi.org/10.7554/eLife.27345

Nagy, G., J.H. Kim, Z.P. Pang, U. Matti, J. Rettig, T.C. Südhof, and J.B. Sørensen. 2006. Different effects on fast exocytosis induced by synaptotagmin 1 and 2 isoforms and abundance but not by phosphorylation. *J. Neurosci.* 26:632–643. https://doi.org/10.1523/JNEUROSCI.2589-05.2006

Nair, D., E. Hosy, J.D. Petersen, A. Constals, G. Giannone, D. Choquet, and J.-B. Sibarita. 2013. Super-resolution imaging reveals that AMPA receptors inside synapses are dynamically organized in nanodomains regulated by PSD95. *J. Neurosci.* 33:13204–13224. https://doi.org/10.1523/JNEUROSCI.2381-12.2013

Pak, C., T. Danko, Y. Zhang, J. Aoto, G. Anderson, S. Maxeiner, F. Yi, M. Wernig, and T.C. Südhof. 2015. Human Neuropsychiatric Disease Modeling using Conditional Deletion Reveals Synaptic Transmission Defects Caused by Heterozygous Mutations in NRXN1. *Cell Stem Cell.* 17: 316–328. https://doi.org/10.1016/j.stem.2015.07.017

Park, H., Y. Li, and R.W. Tsien. 2012. Influence of synaptic vesicle position on release probability and exocytotic fusion mode. *Science.* 335:1362–1366. https://doi.org/10.1126/science.1216937

Peixoto, R.T., P.A. Kunz, H. Kwon, A.M. Mabb, B.L. Sabatini, B.D. Philpot, and M.D. Ehlers. 2012. Transsynaptic signaling by activity-dependent cleavage of neuroligin-1. *Neuron.* 76:396–409. https://doi.org/10.1016/j.neuron.2012.07.006

Perez de Arce, K., N. Schrod, S.W.R. Metzbower, E. Allgeyer, G.K. Kong, A.H. Tang, A.J. Krupp, V. Stein, X. Liu, J. Bewersdorf, et al. 2015. Topographic Mapping of the Synaptic Cleft into Adhesive Nanodomains. *Neuron.* 88: 1165–1172. https://doi.org/10.1016/j.neuron.2015.11.011

Pregno, G., E. Frola, S. Graziano, A. Patrizi, F. Bussolino, M. Arese, and M. Sassoè-Pognetto. 2013. Differential regulation of neurexin at glutamatergic and GABAergic synapses. *Front. Cell. Neurosci.* 7:35. https://doi.org/10.3389/fncel.2013.00035

Prox, J., C. Bernreuther, H. Altmeppen, J. Grendel, M. Glatzel, R. D'Hooge, S. Stroobants, T. Ahmed, D. Balschun, M. Willem, et al. 2013. Postnatal disruption of the disintegrin/metalloproteinase ADAM10 in brain causes epileptic seizures, learning deficits, altered spine morphology, and defective synaptic functions. *J. Neurosci.* 33:12915–12928. https://doi.org/10.1523/JNEUROSCI.5910-12.2013

Reyes, A., R. Lujan, A. Rozov, N. Burnashev, P. Somogyi, and B. Sakmann. 1998. Target-cell-specific facilitation and depression in neocortical circuits. *Nat. Neurosci.* 1:279–285. https://doi.org/10.1038/1092

Rodríguez, C.I., F. Buchholz, J. Galloway, R. Sequerra, J. Kasper, R. Ayala, A.F. Stewart, and S.M. Dymecki. 2000. High-efficiency deleter mice show that FLPe is an alternative to Cre-loxP. *Nat. Genet.* 25:139–140. https://doi.org/10.1038/75973

Rui, M., J. Qian, L. Liu, Y. Cai, H. Lv, J. Han, Z. Jia, and W. Xie. 2017. The neuronal protein Neurexin directly interacts with the Scribble-Pix complex to stimulate F-actin assembly for synaptic vesicle clustering. *J. Biol. Chem.* 292:14334–14348. https://doi.org/10.1074/jbc.M117.794040

Rust, M.J., M. Bates, and X. Zhuang. 2006. Sub-diffraction-limit imaging by stochastic optical reconstruction microscopy (STORM). *Nat. Methods.* 3: 793–796. https://doi.org/10.1038/nmeth929

Saftig, P., and S.F. Lichtenthaler. 2015. The alpha secretase ADAM10: A metalloprotease with multiple functions in the brain. *Prog. Neurobiol.* 135:1–20. https://doi.org/10.1016/j.pneurobio.2015.10.003

Saint-Pol, J., E. Eschenbrenner, E. Dornier, C. Boucheix, S. Charrin, and E. Rubinstein. 2017. Regulation of the trafficking and the function of the metalloprotease ADAM10 by tetraspanins. *Biochem. Soc. Trans.* 45: 937–944. https://doi.org/10.1042/BST20160296

Schreiner, D., T.M. Nguyen, G. Russo, S. Heber, A. Patrignani, E. Ahrné, and P. Scheiffele. 2014. Targeted combinatorial alternative splicing generates brain region-specific repertoires of neurexins. *Neuron.* 84: 386–398. https://doi.org/10.1016/j.neuron.2014.09.011

Schwenk, F., U. Baron, and K. Rajewsky. 1995. A cre-transgenic mouse strain for the ubiquitous deletion of loxP-flanked gene segments including deletion in germ cells. *Nucleic Acids Res.* 23:5080–5081. https://doi.org/10.1093/nar/23.24.5080

Seegar, T.C.M., L.B. Killingsworth, N. Saha, P.A. Meyer, D. Patra, B. Zimmerman, P.W. Janes, E. Rubinstein, D.B. Nikolov, G. Skiniotis, et al. 2017. Structural Basis for Regulated Proteolysis by the α-Secretase ADAM10. *Cell.* 171:1638–1648.e7. https://doi.org/10.1016/j.cell.2017.11.014

Sheng, M., and E. Kim. 2011. The postsynaptic organization of synapses. *Cold Spring Harb. Perspect. Biol.* 3:a005678. https://doi.org/10.1101/cshperspect.a005678

Siddiqui, T.J., and A.M. Craig. 2011. Synaptic organizing complexes. *Curr. Opin. Neurobiol.* 21:132–143. https://doi.org/10.1016/j.conb.2010.08.016

Somogyi, P., G. Tamás, R. Lujan, and E.H. Buhl. 1998. Salient features of synaptic organisation in the cerebral cortex. *Brain Res. Brain Res. Rev.* 26:113–135. https://doi.org/10.1016/S0165-0173(97)00061-1

Sterky, F.H., J.H. Trotter, S.J. Lee, C.V. Recktenwald, X. Du, B. Zhou, P. Zhou, J. Schwenk, B. Fakler, and T.C. Südhof. 2017. Carbonic anhydrase-related protein CA10 is an evolutionarily conserved pan-neurexin ligand. *Proc. Natl. Acad. Sci. USA.* 114:E1253–E1262. https://doi.org/10.1073/pnas.1621321114

Südhof, T.C. 2017. Synaptic Neurexin Complexes: A Molecular Code for the Logic of Neural Circuits. *Cell.* 171:745–769. https://doi.org/10.1016/j.cell.2017.10.024

Suzuki, K., Y. Hayashi, S. Nakahara, H. Kumazaki, J. Prox, K. Horiuchi, M. Zeng, S. Tanimura, Y. Nishiyama, S. Osawa, et al. 2012. Activity-dependent proteolytic cleavage of neuroligin-1. *Neuron.* 76:410–422. https://doi.org/10.1016/j.neuron.2012.10.003

Szoboszlay, M., T. Kirizs, and Z. Nusser. 2017. Objective quantification of nanoscale protein distributions. *Sci. Rep.* 7:15240. https://doi.org/10.1038/s41598-017-15695-w

Tabuchi, K., and T.C. Südhof. 2002. Structure and evolution of neurexin genes: insight into the mechanism of alternative splicing. *Genomics.* 79: 849–859. https://doi.org/10.1006/geno.2002.6780

Tabuchi, K., J. Blundell, M.R. Etherton, R.E. Hammer, X. Liu, C.M. Powell, and T.C. Südhof. 2007. A neuroligin-3 mutation implicated in autism increases inhibitory synaptic transmission in mice. *Science.* 318:71–76. https://doi.org/10.1126/science.1146221

Tang, A.-H., H. Chen, T.P. Li, S.R. Metzbower, H.D. MacGillavry, and T.A. Blanpied. 2016. A trans-synaptic nanocolumn aligns neurotransmitter release to receptors. *Nature.* 536:210–214. https://doi.org/10.1038/nature19058

Treutlein, B., O. Gokce, S.R. Quake, and T.C. Südhof. 2014. Cartography of neurexin alternative splicing mapped by single-molecule long-read mRNA sequencing. *Proc. Natl. Acad. Sci. USA.* 111:E1291–E1299. https://doi.org/10.1073/pnas.1403244111

Uchida, N., Y. Honjo, K.R. Johnson, M.J. Wheelock, and M. Takeichi. 1996. The catenin/cadherin adhesion system is localized in synaptic junctions bordering transmitter release zones. *J. Cell Biol.* 135:767–779. https://doi.org/10.1083/jcb.135.3.767

Ullrich, B., Y.A. Ushkaryov, and T.C. Südhof. 1995. Cartography of neurexins: more than 1000 isoforms generated by alternative splicing and expressed in distinct subsets of neurons. *Neuron.* 14:497–507. https://doi.org/10.1016/0896-6273(95)90306-2

Ushkaryov, Y.A., and T.C. Südhof. 1993. Neurexin III alpha: extensive alternative splicing generates membrane-bound and soluble forms. *Proc. Natl. Acad. Sci. USA.* 90:6410–6414. https://doi.org/10.1073/pnas.90.14.6410

Ushkaryov, Y.A., A.G. Petrenko, M. Geppert, and T.C. Südhof. 1992. Neurexins: synaptic cell surface proteins related to the alpha-latrotoxin receptor and laminin. *Science.* 257:50–56. https://doi.org/10.1126/science.1621094

Ushkaryov, Y.A., Y. Hata, K. Ichtchenko, C. Moomaw, S. Afendis, C.A. Slaughter, and T.C. Südhof. 1994. Conserved domain structure of beta-neurexins. Unusual cleaved signal sequences in receptor-like neuronal cell-surface proteins. *J. Biol. Chem.* 269:11987–11992.

Xiao, B., J.C. Tu, R.S. Petralia, J.P. Yuan, A. Doan, C.D. Breder, A. Ruggiero, A.A. Lanahan, R.J. Wenthold, and P.F. Worley. 1998. Homer regulates the association of group 1 metabotropic glutamate receptors with multivalent complexes of homer-related, synaptic proteins. *Neuron.* 21: 707–716. https://doi.org/10.1016/S0896-6273(00)80588-7

Yan, Q., S.M. Weyn-Vanhentenryck, J. Wu, S.A. Sloan, Y. Zhang, K. Chen, J.Q. Wu, B.A. Barres, and C. Zhang. 2015. Systematic discovery of regulated and conserved alternative exons in the mammalian brain reveals NMD modulating chromatin regulators. *Proc. Natl. Acad. Sci. USA.* 112: 3445–3450. https://doi.org/10.1073/pnas.1502849112

Zhang, P., H. Lu, R.T. Peixoto, M.K. Pines, Y. Ge, S. Oku, T.J. Siddiqui, Y. Xie, W. Wu, S. Archer-Hartmann, et al. 2018. Heparan Sulfate Organizes Neuronal Synapses through Neurexin Partnerships. *Cell.* 174:1450–1464. https://doi.org/10.1016/j.cell.2018.07.002